The Journal of Physiology

A computational model of induced pluripotent stem-cell derived cardiomyocytes incorporating experimental variability from multiple data sources

Divya C. Kernik[1], Stefano Morotti[2], HaoDi Wu[3], Priyanka Garg[3], Henry J. Duff[7], Junko Kurokawa[6], José Jalife[4,5], Joseph C. Wu[3], Eleonora Grandi[2] and Colleen E. Clancy[1]

[1] *Department of Physiology and Membrane Biology, Department of Pharmacology, School of Medicine, University of California, Davis, Davis, CA, USA*
[2] *Department of Pharmacology, School of Medicine, University of California, Davis, CA, USA*
[3] *Stanford Cardiovascular Institute, Department of Medicine, Division of Cardiovascular Medicine, Stanford University School of Medicine, Stanford, CA, USA*
[4] *Department of Internal Medicine, Center for Arrhythmia Research, Cardiovascular Research Center, University of Michigan, Ann Arbor, MI, USA*
[5] *Centro Nacional de Investigaciones Cardiovasculares (CNIC), and CIBERV, Madrid, Spain*
[6] *Department of Bio-Informational Pharmacology, School of Pharmaceutical Sciences, University of Shizuoka, Shizuoka, Japan*
[7] *Libin Cardiovascular Institute of Alberta, Faculty of Medicine, University of Calgary, Calgary, AB, Canada*

Edited by: Harold Schultz & Alicia D'Souza

Linked articles: This article is highlighted in a Journal Club article by Pullinger & Gong. To read this article, visit https://doi.org/10.1113/JP278739.

Key points

- Induced pluripotent stem cell-derived cardiomyocytes (iPSC-CMs) capture patient-specific genotype–phenotype relationships, as well as cell-to-cell variability of cardiac electrical activity
- Computational modelling and simulation provide a high throughput approach to reconcile multiple datasets describing physiological variability, and also identify vulnerable parameter regimes
- We have developed a whole-cell model of iPSC-CMs, composed of single exponential voltage-dependent gating variable rate constants, parameterized to fit experimental iPSC-CM outputs
- We have utilized experimental data across multiple laboratories to model experimental variability and investigate subcellular phenotypic mechanisms in iPSC-CMs
- This framework links molecular mechanisms to cellular-level outputs by revealing unique subsets of model parameters linked to known iPSC-CM phenotypes

Abstract There is a profound need to develop a strategy for predicting patient-to-patient vulnerability in the emergence of cardiac arrhythmia. A promising *in vitro* method to address patient-specific proclivity to cardiac disease utilizes induced pluripotent stem cell-derived

Divya Kernik is currently a PhD candidate in Biomedical Engineering at the University of California, Davis. She obtained a BS in Biomedical Engineering from Johns Hopkins University. The focus of her PhD work has been the development of computational methods that help to understand human-derived cardiac cells, as reported in the present study. In the future, she aims to continue to use computational modelling to address questions in cardiac physiology and pharmacology, with the underlying goal of incorporating human diversity throughout these efforts.

DOI: 10.1113/JP277724

cardiomyocytes (iPSC-CMs). A major strength of this approach is that iPSC-CMs contain donor genetic information and therefore capture patient-specific genotype–phenotype relationships. A cited detriment of iPSC-CMs is the cell-to-cell variability observed in electrical activity. We postulated, however, that cell-to-cell variability may constitute a strength when appropriately utilized in a computational framework to build cell populations that can be employed to identify phenotypic mechanisms and pinpoint key sensitive parameters. Thus, we have exploited variation in experimental data across multiple laboratories to develop a computational framework for investigating subcellular phenotypic mechanisms. We have developed a whole-cell model of iPSC-CMs composed of simple model components comprising ion channel models with single exponential voltage-dependent gating variable rate constants, parameterized to fit experimental iPSC-CM data for all major ionic currents. By optimizing ionic current model parameters to multiple experimental datasets, we incorporate experimentally-observed variability in the ionic currents. The resulting population of cellular models predicts robust inter-subject variability in iPSC-CMs. This approach links molecular mechanisms to known cellular-level iPSC-CM phenotypes, as shown by comparing immature and mature subpopulations of models to analyse the contributing factors underlying each phenotype. In the future, the presented models can be readily expanded to include genetic mutations and pharmacological interventions for studying the mechanisms of rare events, such as arrhythmia triggers.

(Received 18 January 2019; accepted after revision 5 July 2019; first published online 6 July 2019)
Corresponding authors E. Grandi: Department of Pharmacology, School of Medicine, University of California, Tupper Hall, RM 2427, Davis, CA 95616-8636. Email: egrandi@ucdavis.edu and C. E. Clancy: Department of Physiology and Membrane Biology, Department of Pharmacology, School of Medicine, University of California, Davis, Tupper Hall, RM 4303, Davis, CA 95616-8636. E-mail: ceclancy@ucdavis.edu

Introduction

Patient variability is one of the most daunting aspects of forecasting arrhythmia vulnerability in response to inherited disease or drug application. Considerable differences in drug impacts are routinely observed from patient to patient, with significant overlap between normal and pathological variants (Leopold & Loscalzo, 2018). However, genotype, and even sex, have not been sufficiently considered as a biological variable when developing pharmacotherapy regimes (Schwartz *et al.* 1995; Schwartz *et al.* 2001; Shah & Carter, 2008; Jamshidi *et al.* 2012; Kaab *et al.* 2012; Behr & Roden, 2013). There is a profound need to develop a strategy to predict the diverse mechanisms of arrhythmia vulnerability across patient populations.

A promising emerging experimental method utilizes induced pluripotent stem cell-derived cardiomyocytes (iPSC-CMs). iPSC-CMs are an increasingly utilized patient-specific cardiac cell model because they recapitulate cellular electrical properties of normal and diseased phenotypes, preserve patient-specific genotype and demonstrate expected pharmacological responses of adult cardiomyocytes (Moretti *et al.* 2010; Itzhaki *et al.* 2011; Terrenoire *et al.* 2013; Sallam *et al.* 2015). iPSC-CMs derive from adult somatic cells reprogrammed to the embryonic-like state and then differentiated to cardiomyocytes (Takahashi & Yamanaka, 2006). Cell-based models for multiple cardiac diseases have been developed using iPSC-CMs and show the preservation of patient-specific disease markers carried from the source patient to the patient-derived iPSC-CMs (Moretti *et al.* 2010; Itzhaki *et al.* 2011; Lan *et al.* 2013; Garg *et al.* 2018). The retention of patient-specific disease markers makes iPSC-CMs an ideal tool for investigating the patient-specific disease and response. Indeed, iPSC-CMs are currently being utilized in preclinical drug testing and prediction of genotype–phenotype relationships (Sun *et al.* 2012; Lan *et al.* 2013; Liang *et al.* 2013; Navarrete *et al.* 2013; Burridge *et al.* 2016).

One of the limitations of iPSC-CMs as a model of adult cardiac behaviour is their immature phenotype, which more closely resembles fetal cardiomyocytes. The immature iPSC-CM phenotype is characterized by spontaneous beating, significant differences in potassium currents compared to adult cardiac cells and the presence of early-developmental currents (Bett *et al.* 2013; Karakikes *et al.* 2014). Additionally, iPSC-CMs have immature calcium handling as a result of their lack of T-tubules and differences in sarcoplasmic reticulum (SR) calcium handling (Yang *et al.* 2014). Recent experimental developments have enhanced the maturation of iPSC-CMs by mimicking the natural environment, which allows for staged transitions of cardiomyocytes from the embryonic to adult phenotype (Kamakura *et al.* 2013; Nunes *et al.* 2013; Herron *et al.* 2016; Tiburcy *et al.* 2017).

Another persistent concern with iPSC-CM technology has been the vast diversity of phenotypes observed *in*

vitro. One reason for the variability between iPSC-CMs undoubtedly arises from the differences in genetic information of donors (DeBoever *et al.* 2017). Variation as a result of genetic differences is a critical attribute of iPSC-CMs because it allows for the observation of a variety of naturally occurring phenotypes and reflects patient-specific vulnerability to rare events, such as arrhythmia. However, even iPSC-CMs derived from the same donor with identical genetic information may display persistently variable phenotypes as a result of unknown sources of variation. There are a number of potential sources of variability, not least of all the complex process of generating and culturing iPSC-CMs and the influence of precise maturation phases (Narsinh *et al.* 2011). Action potential (AP) morphologies and calcium transients (CaTs) have been shown to vary both within independent laboratories (Doss *et al.* 2012; Du *et al.* 2015) and across laboratories (Hwang *et al.* 2015).

Although the iPSC-CMs that are utilized *in vitro* allow for observation of a variety of responses to drugs and other perturbations, a major drawback in the experimental setting is the lack of a high throughput method to link underlying genomic, proteomic, or ionic mechanisms to the observed whole-cell behaviours. Population-based computational modelling provides a powerful tool in closing this gap via *in silico* analysis of variability in cardiac electrophysiology (Muszkiewicz *et al.* 2016; Yang *et al.* 2016; Passini *et al.* 2017; Ni *et al.* 2018). Implementation of these approaches in the modelling and simulation of iPSC-CMs has the potential to reconcile multiple datasets, define physiological ranges of variability and identify vulnerable parameter regimes (Sarkar & Sobie, 2010; Yang & Clancy, 2012; Britton *et al.* 2013; Yang *et al.* 2015; Morotti & Grandi, 2017). With respect to using iPSC-CMs for cardiotoxicity testing of pharmacological interventions, the US Food and Drug Administration has outlined the Comprehensive In Vitro Proarrhythmia Assay (CiPA) protocol for combining cellular iPSC-CM outputs with computational approaches (Fermini *et al.* 2016). These efforts will be further strengthened by a high throughput computational approach to study the mechanisms underlying phenotypic variability in iPSC-CMs.

Although prior studies have addressed computational modelling of iPSC-CMs (Paci *et al.* 2013; Koivumaki *et al.* 2018), there is a need for a computational model which incorporates the wide-range of experimental measurements from iPSC-CMs. Paci *et al.* (2013) have developed a computational model of the iPSC-CM that is based on a single iPSC-CM experimental electrophysiology study. As a result of the lack of experimental data available at the time, the model is largely based on *I–V* curves measured in iPSC-CMs by Ma *et al.* (2011). Model kinetics were largely retained from the adult ventricular model of ten Tusscher *et al.* (2004), with any additional changes based on experimental data from animal or adult human cells (ten Tusscher *et al.* 2004; Paci *et al.* 2012). Although this model captures the spontaneously beating iPSC-CM AP phenotype, it is based on a limited description of iPSC-CM behaviour. Later iterations of iPSC-CM models by Paci *et al.* (2018) and Koivumaki *et al.* (2018) incorporated modifications to improve calcium handling; however, these adaptations were made with limited experimental data to define the range of calcium transient behaviour during the AP. The model presented in this study is constrained by several calcium handling datasets that have not been utilized in parameterizing prior models, including concentration measurements of the iPSC-CM calcium transient during the AP.

Other computational studies have adapted the framework of Paci *et al.* (2018) to model specific phenotypes and populations of iPSC-CMs (Lei *et al.* 2017; Paci *et al.* 2017; Koivumaki *et al.* 2018; Paci *et al.* 2018; Tveito *et al.* 2018); however, none of these efforts have utilized *in vitro* kinetics data to implement experimentally informed variation of iPSC-CMs. There is a wide range iPSC-CM phenotypes that are not captured by previous approaches to modelling iPSC-CMs. Because there is a wide range of 'normal' iPSC-CM behaviours characterized by distinct experimental laboratories, we present a comprehensive computational model that captures this experimental variability.

The goal of the present study is to extend the iPSC-CM technology by developing an *in silico* complement: a high throughput method for analysing phenotypic mechanisms of emergent behaviours in normal control iPSC-CMs. This is achieved by computationally modelling phenotypic variability in control iPSC-CMs via simple models based on source data from multiple laboratories. The use of simplified models to describe ionic gating kinetics allows us to fully parameterize a model to fit multiple individual experimental datasets. This approach allowed for the rapid construction of model populations from multiple data sets, at the same time as setting the stage for future expansion into patient specific electrophysiology models by allowing reparameterization from data collected from donor cells.

Additionally, this allows us to investigate whether kinetic variability can explain whole-cell variation observed in iPSC-CMs experimentally. Here, we show that predicted experimental variability at the subcellular level can recapitulate the full range of *in vitro* whole-cell iPSC-CM behaviour in an *in silico* cellular population. The population can further be used to identify subpopulations of interest, including immature and mature phenotypes, and clarify the underlying processes that characterize the phenotypes. In the future, our approach can also be used to examine mechanism of disease and drug effects. The computational models of iPSC-CMs will allow for identification of parameter regimes with

increased proclivity to arrhythmia in the presence of genetic mutation or pharmacological intervention. The tools may be applied for *in silico* screening and prediction of drug effects on varied genetic backgrounds to predict patient pharmacological responses.

Methods

All source code and instructions are freely available on the GitHub (https://github.com/ClancyLabUCD/IPSC-model).

Model construction

As in prior cardiomyocytes models (Rudy & Silva, 2006), the iPSC-CM can be described by the differential equation:

$$\frac{dV}{dt} = \frac{-I_{\text{ion}} + I_{\text{stim}}}{C_{\text{m}}} \quad (1)$$

where V is voltage, t is time, C_{m} is membrane capacitance, I_{ion} is the sum of transmembrane currents and I_{stim} is the stimulus current ($I_{\text{stim}} = 0$ pA/pF in spontaneously beating cells). The iPSC-CM model (schematic representation in Fig. 1, left) includes 13 transmembrane currents, such that:

$$I_{\text{ion}} = I_{\text{Na}} + I_{\text{CaL}} + I_{\text{Kr}} + I_{\text{Ks}} + I_{\text{K1}} + I_{\text{to}} + I_{\text{f}} + I_{\text{CaT}} + I_{\text{NCX}} + I_{\text{PMCA}} + I_{\text{NaK}} + I_{\text{bCa}} + I_{\text{bNa}} \quad (2)$$

A schematic of the model cell containing all the ionic processes and compartments in the model is shown in Fig. 1. Seven key transmembrane currents (I_{Na}, I_{CaL}, I_{Kr}, I_{Ks}, I_{K1}, I_{to} and I_{f}, indicated by red stars in Fig. 1), were reformulated using Hodgkin–Huxley-type gating formulations (Hodgkin & Huxley, 1952). For each of these currents, single exponential rate-constants (Fig. 1, right) were optimized to iPSC-CM experimental data (Fig. 2, step 1a). The remaining currents shown in Fig. 1 were modelled using formulations from previously published cardiac models (Shannon *et al.* 2004; ten Tusscher *et al.* 2004; Maltsev & Lakatta, 2009), and tuned to recapitulate experimental data for whole-cell outputs of iPSC-CMs. Details describing the experimental data used and resulting model formulations are provided in the Results.

The iPSC-CM ion dynamics were formulated as performed previously (DiFrancesco & Noble, 1985; Luo & Rudy, 1994; ten Tusscher *et al.* 2004), assuming rapid equilibrium approximation for calcium buffers in various compartments:

$$\frac{dCa_{\text{i}}}{dt} = Ca_{\text{Buf,c}} \times \left[-\frac{I_{CaL,Ca} + I_{CaT} + I_{PMCA} + I_{bCa} - 2I_{NCX}}{2V_cF} + J_{\text{Rel}} - J_{\text{up}} + J_{\text{leak}} \right] \quad (3)$$

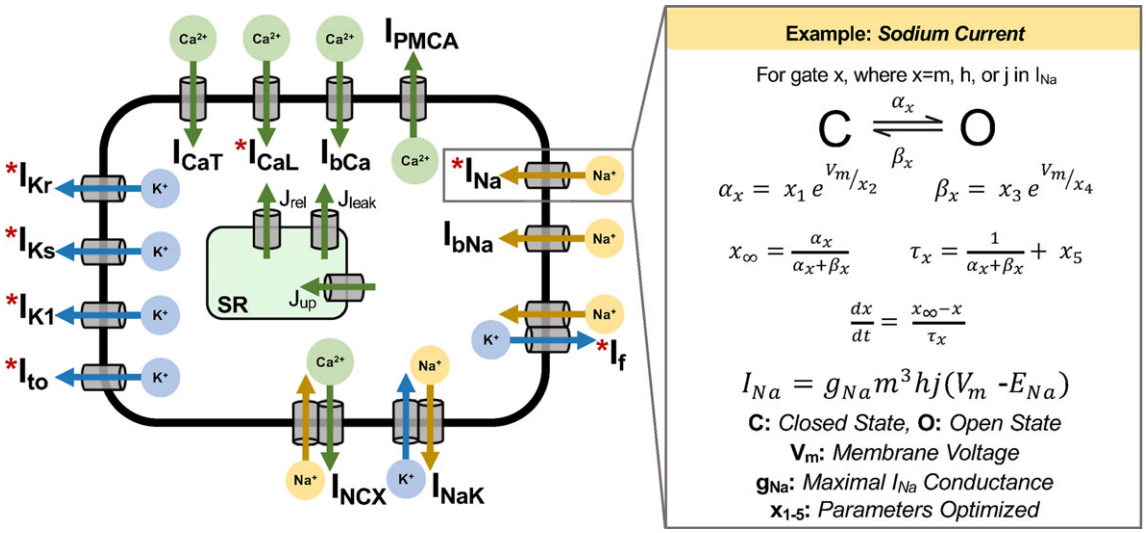

Figure 1. A schematic of the computational iPSC-CM model
Red stars indicate individual currents (*I_{Na}, I_{CaL}, I_{Kr}, I_{Ks}, I_{K1}, I_{to} and I_{f}), formulated using single-exponential voltage-dependent rate constants. Parameters were optimized to experimental iPSC-CM kinetic data. The mathematical formulation for an example current, I_{Na}, is shown on the right. All gating variables in the starred currents were modelled using the example formula for gating variable x. Additional calcium-dependent currents (I_{NCX}, I_{PMCA}, I_{CaT} and SR currents: I_{SERCA}, I_{RyR} and I_{leak}) were modelled using previously published model formulations, optimized to calcium transient data from iPSC-CMs. Remaining currents (I_{NaK}, I_{bCa}, I_{bNa}) were modelled using ten Tusscher 2004 formulations optimized to recapitulate iPSC-CM AP data.

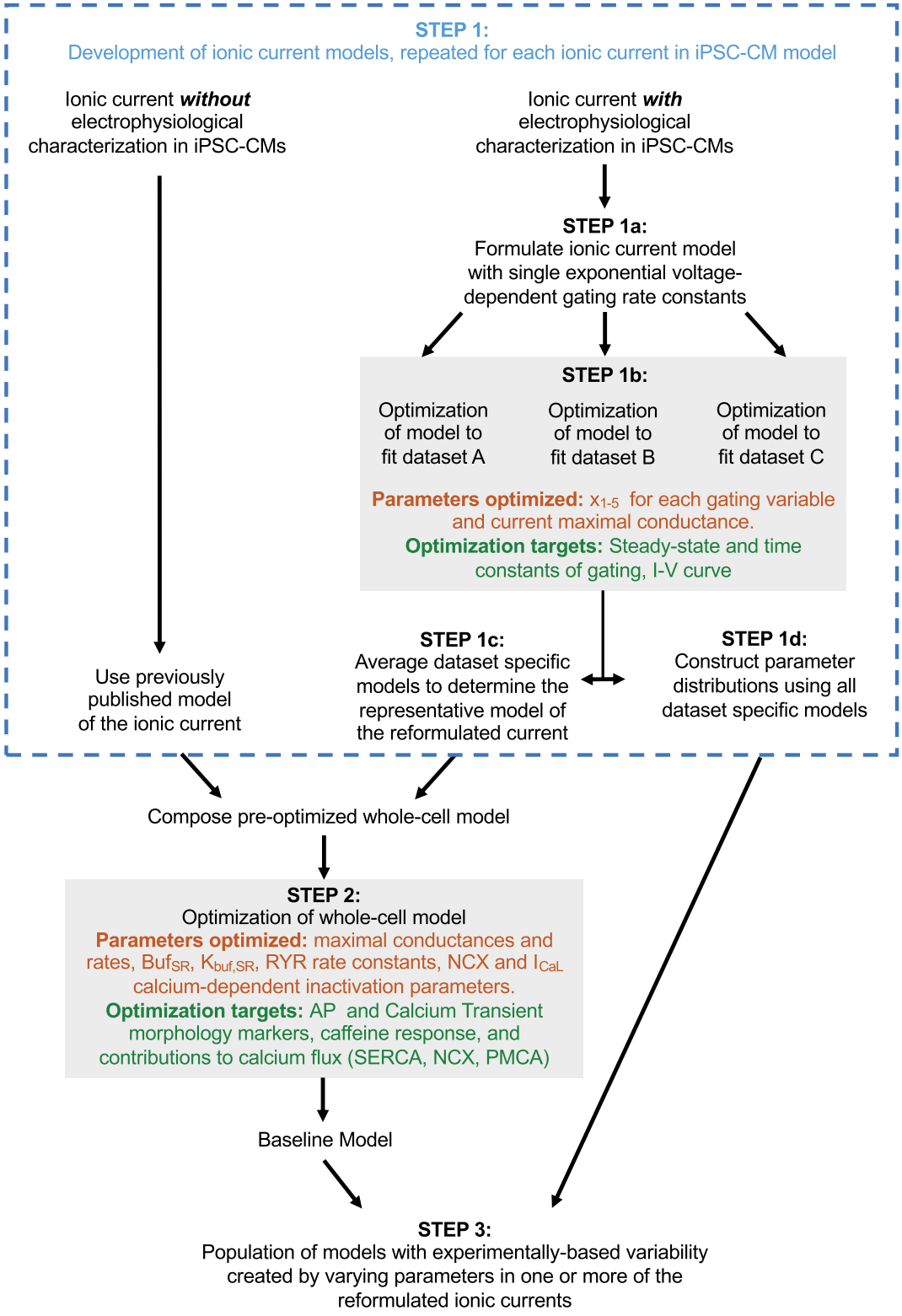

Figure 2. Flow chart
Flow chart showing the methodology for building the iPSC-CM model populations.

$$\frac{dCa_{SR}}{dt} = Ca_{Buf,SR} * \frac{V_c}{V_{SR}}(-J_{Rel} + J_{Up} - J_{leak}) \quad (4)$$

$$Ca_{Buf,X} = \frac{1}{1 + \frac{Buf_x * K_{Buf,X}}{([Ca]_X + K_{Buf,X})^2}},$$

$$\text{for } X = \text{cytoplasm } (C),\ \text{sarcoplasmic reticulum (SR)} \quad (5)$$

$$\frac{dNa_i}{dt} = -\frac{I_{Na} + I_{f,Na} + I_{CaL,Na} + I_{bNa} + 3I_{NCX} + 3I_{NaK}}{V_c F} \quad (6)$$

$$\frac{dK_i}{dt} = -\frac{I_{Kr} + I_{Ks} + I_{K1} + I_{to} + I_{f,K} + I_{CaL,K} - 2I_{NaK} + I_{stim}}{V_c F} \quad (7)$$

where F is the Faraday constant, V_C is the cytoplasmic volume, V_{SR} is the sarcoplasmic reticulum volume, Buf_X is the total buffer concentration in a given compartment and $K_{Buf,X}$ is the half-saturation constant of the buffer in a given compartment. Total volume and cytoplasmic buffering constants in the iPSC-CM model were set to experimental measurements in iPSC-CMs from ($V_{total} = V_C + V_{SR} = 3960\ \mu m^3$, $Buf_C = 0.06$ mM and $K_{Buf,C} = 0.0006$ mM) (Hwang *et al.* 2015). Remaining SR buffering parameters (Buf_{SR}, $K_{Buf,SR}$) were optimized in the whole-cell optimization (Fig. 2, Step 2). Relative proportions of volumes (V_C:V_{SR}), were retained from the adult human ventricular model by ten Tusscher *et al.* (2004), referred to as the ten Tusscher 2004 model. Capacitance of the cell was set to 60 pF, based on the experimentally observed range in iPSC-CMs (18–89 pF) (Ma *et al.* 2011; Hwang *et al.* 2015; Li *et al.* 2017).

The models were implemented in MATLAB, version R2017a (MathWorks Inc., Natick, MA, USA) and solved using ode15s.

AP morphology

APs in the baseline model and populations were evaluated by computing a series of AP morphology markers. Maximum diastolic potential (MDP) was the most negative voltage during the AP. Maximal upstroke velocity (dV/dt_{max}) was the maximal slope between two points in the computed AP upstroke. AP amplitude (Amp) was calculated as the difference in voltage between MDP and the peak voltage during the AP. AP duration (APD_x) was the time between dV/dt_{max} and X% AP repolarization from the peak voltage (e.g. For APD_{90}, time from dV/dt_{max} to $V_m = \text{Peak} - 0.9*\text{Amp}$).

Parameter optimization of reformulated ionic channel models (Fig. 2, step 1b)

For each of the reformulated currents, model parameters were optimized to multiple experimental datasets, resulting in dataset-specific parameterization instances of the model. For each dataset-specific model, external ion concentrations and voltage protocols were set to reflect the corresponding experimental conditions. Experimental conditions for each dataset are described in Table 1. All of the experimental data used to optimize the models were collected in iCell iPSC-CMs at physiological temperature (37°C), unless otherwise specified (in which cases, data were temperature-corrected with appropriate Q_{10} values, as specified in the Results for the corresponding ionic current). This process was used to generate dataset-specific models. As an example, consider three separate experimental iPSC-CM datasets for a given current: datasets A, B and C. In the case of the sodium current (Fig. 3), this would refer to (A) Ma *et al.* (B) Jalife Immature, (C) Jalife Mature.

Considering gating variable x in Fig. 1, parameters x_{1-5} were optimized to recapitulate the experimental kinetics for gate x. In Fig. 2, this is shown as Step 1b in the upper highlighted box indicating the optimization routine. Parameter optimization minimized the error between the model and experimental voltage-dependence of the steady-state and time constants of a given gate. The error function was the sum of the log squared difference between the data and model fit, normalized to the size of the dataset. The 'fminsearch' function was used in MATLAB to implement Nelder–Mead minimization of the error function. Random small perturbations (<10%) were applied to resulting local minima, to improve data fit. The parameter fit with the minimal error function value after 100 perturbations was used as the optimal model fit to the data. This is a relatively simple approach which only requires standard MATLAB functions, allowing for additional dataset-specific models to be easily obtained and incorporated into the model in the future. Additionally, this approach has been previously utilized for optimization of more complex ionic current models and datasets (Moreno *et al.* 2016). The ionic current models in the present study were chosen to minimize the number of optimized parameters, thus this approach was sufficient to successfully fit the models to the datasets presented.

These simplified models also allow for a more physiological understanding of model parameterizations. The ionic current model parameters can be combined such that:

$$x_\infty = \frac{\alpha_x}{\alpha_x + \beta_x} = \frac{1}{1 + \frac{\beta_x}{\alpha_x}} = \frac{1}{1 + \frac{x_3 e^{V/x_4}}{x_1 e^{V/x_2}}} = \frac{1}{1 + x_6 e^{\frac{V}{x_7}}} \quad (8)$$

Table 1. Experimental conditions for all datasets used in optimization of ionic current models

					Extracellular (mM)				Intracellular (mM)					
	Reference	Temperature	n =	Cell-line	NaCl	KCl	$CaCl_2$	NMDG	KCl	K-gluconate	K-aspartate	NaCl	$CaCl_2$	Na2-ATP
INa	Ma *et al.* (2011)	35–37	5	iCell	50		1.8					10	2	
	Herron *et al.* (2016) (PDMS/glass)	21–22	19/12	iCell	20		1.8					5		
	Kurokawa Lab (Li *et al.*, 2017)	25	5	iCell	30		2							5
ICaL	Es-Salah-Lamoureux *et al.* (2016)	room	15–17	IHC			5					5	2	
	Veerman *et al.* (2016)	36	21	IHC			1.8							
	Ma *et al.* (2011)	room	5	iCell			5					5	2	
ICaT	Kurokawa Lab (Li *et al.*, 2017)	36	2	iCell			5							5
IKr	Bellin *et al.* (2013)	37	14	IHC	140	5.4	1.8		20	125				
	Es-Salah-Lamoureux *et al.* (2016)	35	21	IHC	140	4	1		20	125				
	Ma *et al.* (2011)	35–37	8	iCell	150	5.4	1.8		150			5	2	
	Wu Lab (Garg *et al.* 2018)	36–37	4	IHC	150	5.4	1.8		120					
Ito	Veerman *et al.* (2016)	36	13	IHC	140	5.4	1.8		20	105		5		
	Cordeiro *et al.* (2013)	36	14	iCell	126	5.4	2		10		125	10	5	
	Ma *et al.* (2011)	35–37	8	iCell		5.4		160		150			5	
IKs	Ma, Wei *et al.* (2015)	37	7/8	IHC/iCell	140	5.4	1.7		50		80			
	Ma *et al.* (2011)	35–37	5	iCell	150	5.4	1.8		20		125			
If	Kurokawa Lab (Li *et al.* 2017)	36	9	iCell	135	5.4	1.8		30				1	
	Ma *et al.* (2011)	35–37	17	iCell	135	5.4	1.8		150			5	2	
IK1	Ma *et al.* (2011)	35–37	4	iCell		5.4		160		150				
	Herron *et al.* (2016) (PDMS/glass)	21–22	5/7	iCell	148	5.4	1.8		148					
	Kurokawa Lab (Li *et al.* 2017)	36	7	iCell	135	5.4	1.8		20				1	

*IHC, in-house control cell-line.

where:

$$x_6 = \frac{x_3}{x_1}, \quad x_7 = \frac{1}{\left(\frac{1}{x_4} - \frac{1}{x_2}\right)} \tag{9}$$

With this simplification, we can understand the parameter effect on the voltage dependence of steady-state behaviour. The x_∞ function has a sigmoidal voltage-dependence which is characterized by the slope and V_{half}, where $x_\infty(V_{half}) = 0.5$. Using the parameter combinations shown in eqn (8), x_6 and x_7 are proportional to V_{half} and slope, respectively.

Constructing the average parameter set for reformulated currents (Fig. 2, step 1c)

Consider parameter x_1 in any gating variable. The value of x_1 is determined via parameter optimization to an experimental dataset. If three experimental datasets (datasets A, B and C) are used, then each dataset corresponds to a unique parameter value of x_1 (x_{1A}, x_{1B}, x_{1C}) in each dataset-specific model. The baseline model is composed of average parameters values for x_1, such that:

$$x_{1,avg} = \frac{x_{1A} + x_{1B} + x_{1C}}{3} \tag{10}$$

This is repeated for each parameter in the ionic current model. These averaged parameters ($x_{1-5,avg}$, $g_{x,avg}$) comprise an average model for each current. The baseline model for each current was constructed using the average model gating kinetics. The baseline model is the starting point to implement variability.

Constructing the parameter distributions for reformulated currents (Fig. 2, step 1d)

To create a population of models that capture variability between the dataset-specific models, we created a distribution for each parameter in the reformulated currents. This distribution is centred at the baseline ionic current model value. Similar to our approach in selecting an optimization method (Fig. 2, step 1b), the sampling method was chosen for simplicity and to allow for variation in a large number of parameters. Although the range of variability was determined by the range of the experimental datasets used to in form the model, there is still insufficient data to accurately determine to distribution of data between these datasets (constructing the distribution of experimental data would require more data than the two to five datasets per ionic current used in this study). For simplicity we used a normal distribution of parameters, and randomly selected the parameter values in building the population of models.

For example, for each cell in the population of models, the value of x_1 is randomly chosen from a normal distribution around $x_{1,avg}$. The normal distribution is created using $x_{1,avg}$ and the SD of x_{1A}, x_{1B} and x_{1C}, as described above. This same process is used to create a distribution for each parameter (x_{1-5}) in each model gating variable, and for the maximal conductance (g_x).

Optimization of the baseline whole-cell model (Fig. 2, step 2)

The pre-optimized whole cell model is composed of average parameter sets for the reformulated currents combined with non-reformulated currents from existing models in the whole-cell model structure and geometry as described above. To tune parameters in non-reformulated

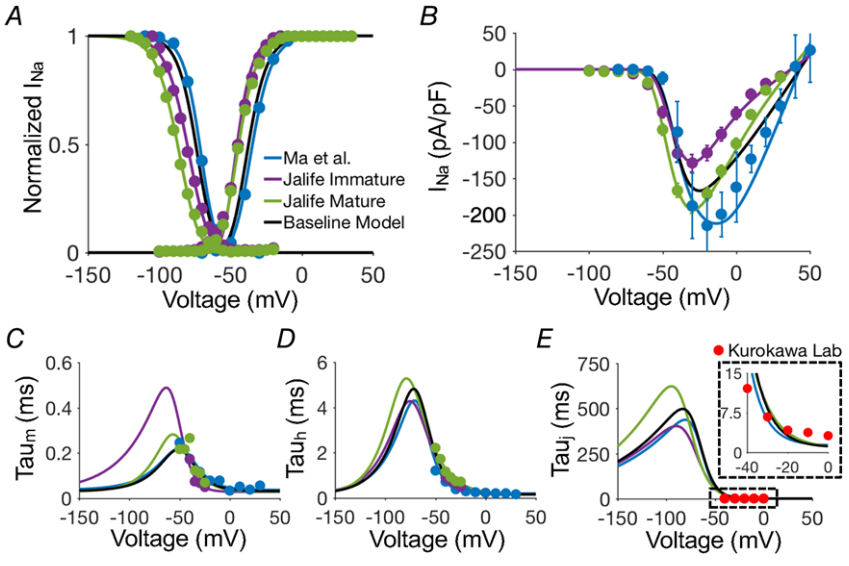

Figure 3. Sodium current (I_{Na}) model optimization
A, steady-state inactivation and activation curves. Dataset-specific model fits (lines) optimized to experimental data (points). The sodium current model used in the baseline whole-cell model is shown in black. Colours represent distinct experimental iPSC-CM data from Ma *et al.* (2011) and from immature and mature cell preparations from the Jalife lab (Herron *et al.* 2016). *B*, *I–V* curves for I_{Na}. Dataset-specific models were simulated using the experimental conditions of the corresponding experimental data. *C*, I_{Na} activation (*m*-gate) time constants. *D*, I_{Na} fast-inactivation (*h*-gate) time constants. *E*, I_{Na} slow-inactivation (*j*-gate) time constants. *j*-gate time constant parameters for all I_{Na} models were optimized to experimental iPSC-CM data from the Kurokawa lab (Li *et al.* 2017).

currents, as well as calcium handling parameters that were not directly defined by experiments, we implemented an optimization of the whole-cell model. This is shown in Fig. 2, step 2, the second highlighted optimization routine in the flowchart.

To optimize the whole-cell model, 'fminsearchbnd' function was used in MATLAB to implement Nelder–Mead minimization of the error function. This 'bound' version of the Nelder–Mead algorithm was used to maintain the reformulated maximal conductances within a ±20% range of $g_{x,avg}$ from the pre-optimized baseline model. The maximal conductance of the reformulated currents, maximal conductances and fluxes of the remaining currents, SR buffering constants, calcium-dependent inactivation in I_{CaL}, RYR rate constants and NCX kinetic parameters were optimized to fit whole-cell behaviour within the experimentally observed range for iPSC-CMs. As in the optimization of the ionic currents, the error function was defined as the sum of the log squared difference between the experimental data and whole-cell model output. The targets for the optimization function considered the experimentally observed range of AP morphology (MDP, APD_{90}, AP amplitude, maximal upstroke velocity), CaT morphology (time constant of decay, time to peak, ratio of time constant of decay and time to peak, CaT amplitude and diastolic $[Ca^{2+}]$), calcium handling response to caffeine (peak calcium and decay, not shown) (Hwang *et al.* 2015) and contribution of SERCA, NCX and PMCA to calcium efflux from the cytosol.

The ionic current models shown as black lines in Figs 3–9 are the final version of each current model, including all tuning of maximal conductance in the whole-cell optimization. The baseline model resulting from this optimization was used as the starting point for all subsequent populations. All parameters which were not randomized in the model populations (remaining currents, cell geometry, etc.) were kept at the baseline model values.

Sensitivity analysis

To further analyse the baseline models (Figs 11*E* and 15*C*), parameter sensitivity was conducted using multivariable linear regression (Sobie, 2009). Sensitivity analysis was conducted based on variation of the maximal conductance and maximal ion transport rates of the transmembrane currents (I_{Na}, I_{CaL}, I_{CaT}, I_{Kr}, I_{Ks}, I_{K1}, I_{to}, I_f, I_{NCX}, I_{NaK}, I_{PMCA}, I_{bNa} and I_{bCa}) and SR fluxes (J_{Up}, J_{Rel} and J_{leak}). The remaining parameters, including all parameters describing model kinetics, were held at the baseline model values. Random scaling factors were chosen from

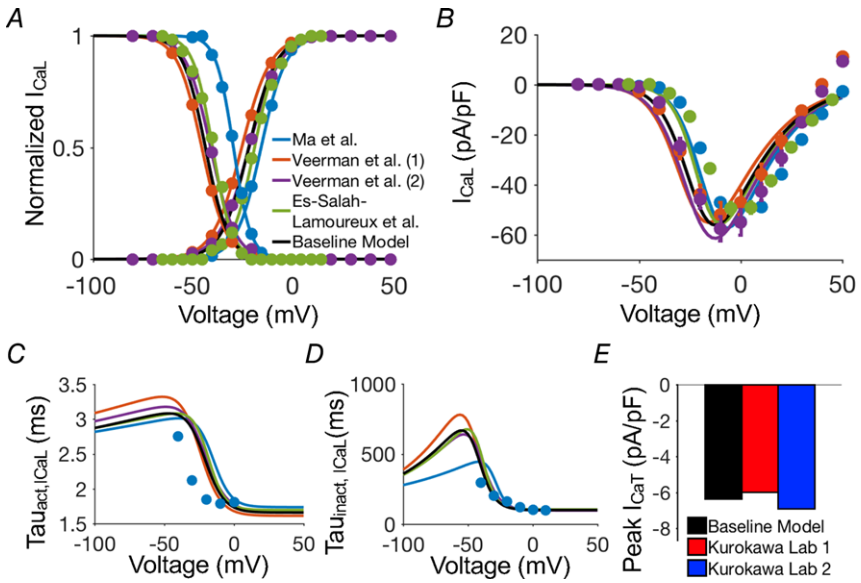

Figure 4. Calcium current model optimization
A, L-type calcium current (I_{CaL}) steady-state inactivation and activation curves with dataset-specific model fits (lines) optimized to experimental data (points). The L-type calcium model used in the baseline cellular model is shown in black. Coloured symbols represent experimental iPSC-CM data from Ma *et al.* (2011), Veerman *et al.* (2016) and Es-Salah-Lamoureux *et al.* (2016). *B*, *I–V* curves for I_{CaL}. Calcium-dependent gating model formulation retained from ten Tusscher 2004 adult cardiomyocyte model with parameter optimization to fit whole cell iPSC-CM outputs. *C*, time constants of I_{CaL} activation gate. Time constant parameters for all I_{CaL} models were optimized to experimental iPSC-CM data from Ma *et al.* (2011). *D*, time constants of I_{CaL} inactivation gate. *E*, optimization of peak T-type calcium current (I_{CaT}) to experimental iPSC-CM data from the Kurokawa lab (Li *et al.* 2017). Model formulation of I_{CaT} was retained from the Maltsev and Lakatta sinoatrial node model.

a log-normal distribution with a median value of 1, SD of 0.1. In total, 5000 randomly parameterized models were run for each sensitivity analysis shown. For the baseline population (Fig. 11*E*; immature in Fig. 15*C*) only spontaneously beating, AP generating, models were analysed. This resulted in 89.3% model retention rate. For the mature population, only stimulated beating, AP generating, models were analysed. This resulted in 67.2% model retention rate. For each analysis shown, 50 randomly determined subpopulations of 1000 models were analysed, resulting in a SD of less than 0.025 for all regression bars shown. Each cell simulation was run until there was a $<1\%$ change in minimum ion concentration (for Ca_i, Ca_{SR}, Na_i and K_i) between the first and last beat during a 50 s simulation run. Once the steady-state criteria were met (ranging from 60 to 600 s), the final AP was saved for regression analysis.

Development of population-based models based on experimental variability (Fig. 2, step 3)

To create a population of models (as shown in Figs 12, 13 and 16), the parameters of the varied currents were randomly determined using the parameter distributions created from the dataset-specific models. Each parameter was chosen from a distribution centered at the baseline model value. For example, for each cell in the population of models the value of x_1 is randomly chosen from a normal distribution around $x_{1,avg}$. The normal

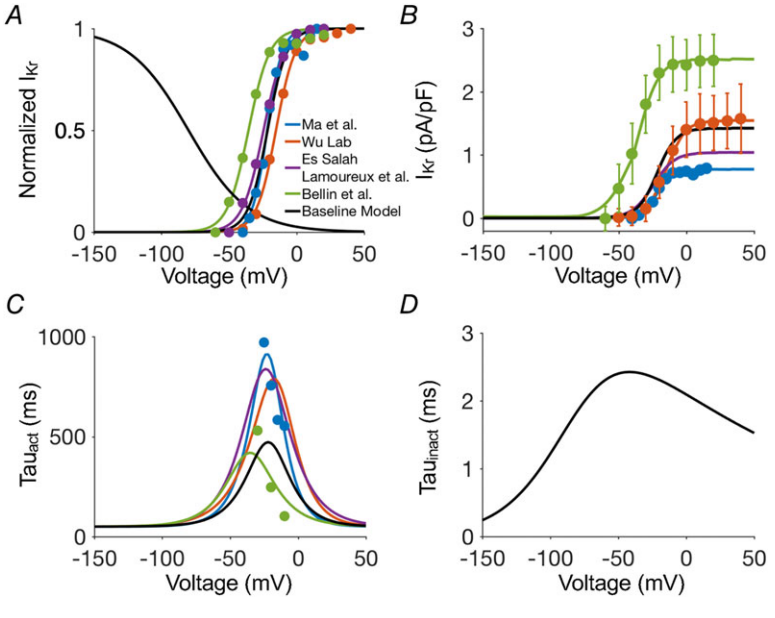

Figure 5. Rapid delayed rectifier potassium current (I_{Kr}) model optimization
A, steady-state activation with dataset-specific model fits (lines) optimized to experimental data (points). The I_{Kr} model used in the baseline cellular model is shown in black. Coloured symbols represent experimental iPSC-CM data from Ma *et al.* (2011), the Wu lab (Garg *et al.* 2018), Es-Salah-Lamoureux *et al.* (2016) and Bellin *et al.* (2013). For I_{Kr} inactivation gating, existing ten Tusscher 2004 model components were reformulated to single exponential forms. *B*, *I–V* curves for I_{Kr}.*C*, time constants of the I_{Kr} activation gate. Activation time constants for the models of Ma *et al.* (2011), the Wu lab (Garg *et al.* 2018) and Es-Salah-Lamoureux *et al.* (2016) were optimized to experimental iPSC-CM data from Ma *et al.* (2011). *D*, time constants of I_{Kr} inactivation gate using the ten Tusscher 2004 model reformulated to single exponential forms.

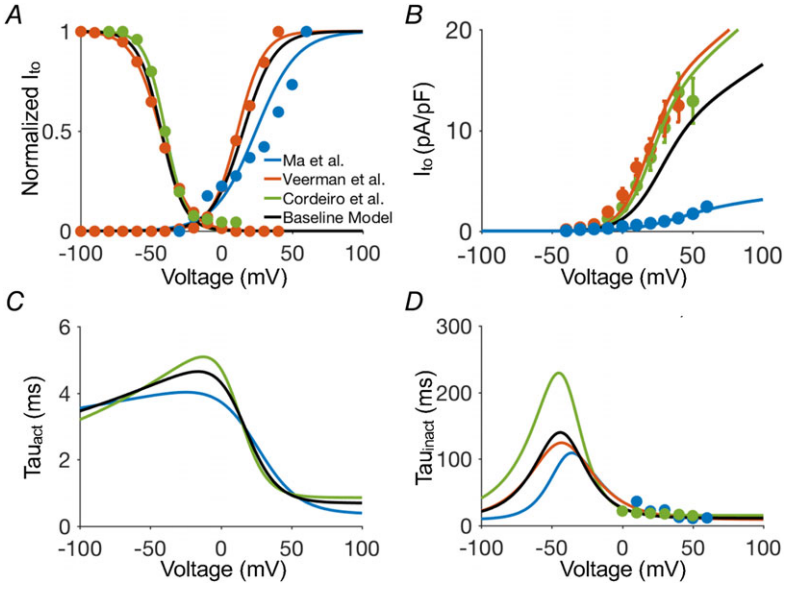

Figure 6. Transient outward potassium current (I_{to}) model optimization
A, steady-state activation and inactivation curves with dataset-specific model fits (lines) optimized to experimental data (points). The I_{to} model used in the baseline cellular model is shown in black. Coloured symbols represent experimental iPSC-CM data from Veerman *et al.* (2016), Ma *et al.* (2011) and Cordeiro *et al.* (2013). *B*, *I–V* curves for I_{to}. *C*, time constants of I_{to} activation gate. For activation time constants in all I_{to} models, the ten Tusscher 2004 I_{to} activation time constants were reformulated to single exponential forms. *D*, time constants of I_{to} inactivation gate. Model time constant parameters of Veerman *et al.* (2016) were optimized to iPSC-CM experimental data from Ma *et al.* (2011).

distribution is created using $x_{1,avg}$ and the SD of x_{1A}, x_{1B} and x_{1C}, as described above (Fig. 2, step 1c). This same process is used to create a distribution for each parameter (x_{1-5}) in each model gating variable, as well as for the maximal conductance (g_x). The populations are constructed by randomly selecting each parameter from these distributions. In the single-current variation populations, all parameters for the chosen current are randomly determined and the remaining model currents retain the baseline model formulation. In the final population, parameters for all five varied currents (I_{Na}, I_{CaL}, I_{Kr}, I_{K1} and I_f) are randomly selected from the constructed distributions.

Experimental calcium imaging (Wu Lab)

iPSC-CMs were disassociated by Accutase and seeded in Matrigel-coated (Becton-Dickinson Biosciences, Franklin Lakes, NJ, USA) coverslips at a density of 20 000 cells well^{-1}. After recovery, cells were loaded with 5 μM Fura-2 AM in Tyrode's solution (140 mM NaCl, 5.4 mM KCl, 1 mM $MgCl_2$, 10 mM glucose, 1.8 mM $CaCl_2$ and 10 mM Hepes, pH 7.4, with NaOH at room temperature) for 10 min in incubator, and were then washed with pre-warmed Tyrode's solution three times. Cells were paced at 0.5 Hz during recording. For Fura-2 AM imaging, calcium signals were sampled using a custom-made Eclipse Ti-E inverted microscope (Nikon, Tokyo, Japan) with a 40× oil immersion objective (NA 0.95) and a Lambda DG-4 ultra-high speed wavelength switching light source (Sutter Instruments, Novato, CA, USA). Signals were collected with iXon Ultra 897 EMCCD (Andor Technology Ltd, Belfast, UK) as high-frame-rate video (512 × 512, 50 frames s^{-1}). Custom-made IDL (interactive digital language) script was used for data analysis. Calcium signal intensity was expressed F340/380 in Fura-2 AM recording. For each cell line, we recorded at least 30 cells from two batches of differentiation.

Experimental electrophysiology recordings (Kurokawa Lab)

The methods for I_{K1}, I_{Na} and I_f experimental data used to optimize the model are as described previously in Li *et al.* (2017). The methodology for the I_{CaT} recordings is described here.

Cell culture (Kurokawa Lab). We used commercially available human iPS cell (hiPSC)-derived cardiomyocytes, iCell-cardiomyocytes (Cellular Dynamics International

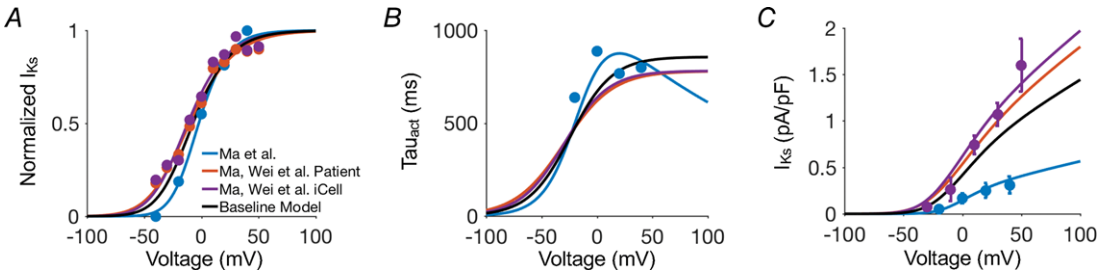

Figure 7. Slow delayed rectifier potassium current (I_{Ks}) model optimization
A, steady-state activation with dataset-specific model fits (lines) optimized to experimental data (points). The I_{Ks} model used in the baseline cellular model is shown in black. Coloured symbols represent experimental iPSC-CM data from Ma *et al.* (2011) and two separate iPSC-CM cell-line datasets in Ma *et al.* (2015). *B*, time constants of the I_{Ks} activation gate. Time constants for all I_{Ks} models were optimized to experimental iPSC-CM data from Ma *et al.* (2011). *C*, *I–V* curves for I_{Ks}.

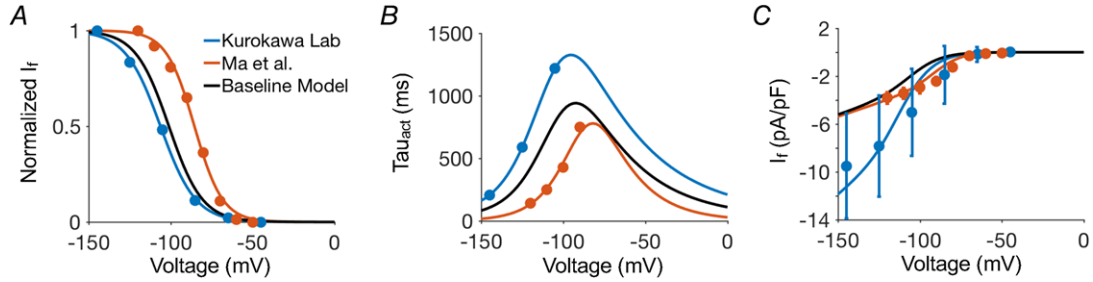

Figure 8. Pacemaker/funny current (I_f) model optimization
A, steady-state activation with dataset-specific model fits (lines) optimized to experimental data (points). The I_f model used in the baseline cellular model is shown in black. Coloured symbols represent experimental iPSC-CM data from the Kurokawa lab (Li *et al.* 2017) and Ma *et al.* (2011). *B*, time constants of the I_f inactivation gate. *C*, *I–V* curves for I_f.

Japan, Tokyo, Japan). Pre-cultured iCell-cardiomyocytes obtained according to the company manual were dissociated enzymatically and were cultured onto laminin/poly-D/L-lysine-coated glass bottom dishes. These re-plated cells started to beat within 48 h. Electrophysiological experiments were performed within 2 weeks after thawing because the distributing company (Cellular Dynamics International Japan) warrants preservation of a high purity in the user's guide.

Electrophysiology (Kurokawa Lab). Membrane currents were recorded with the perforated configuration of the patch clamp technique using an Axopatch 200B amplifier (Molecular Devices, Sunnyvale, CA, USA). Signals were low-pass filtered at 5 kHz, and sampled at 2–5 kHz. No correction for the liquid junction potential was made. pCLAMP, version 9.2 or 10.02 (Molecular Devices, Sunnyvale, CA, USA) was used to generate voltage-pulse protocols, as well as for acquisition and analysis of data.

Cultured cells were placed on the stage of the inverted microscope (IX-71; Olympus, Tokyo, Japan) and the culture medium was replaced by a Tyrode's solution (135 mM NaCl/0.33 mM NaH_2PO_4/5.4 mM KCl/1.8 mM $CaCl_2$/0.53 mM $MgCl_2$/5.5 mM glucose/5 mM Hepes, pH 7.4). After the giga-ohm seal formation, the Tyrode's solution was used to replace the external recording solution for each membrane current using a rapid perfusion system (time constant; >20 ms) (Kurokawa *et al.* 2001). Each of the patch clamp data samples was obtained from an individual culture dish. Experiments were performed at 36 ± 1 °C.

During the recordings of $I_{Ca,T}$, external Na^+ ions and all K^+ ions were replaced by tetraethyl ammonium $(TEA)^+$ and Cs^+ ions to suppress both Na^+ currents and K^+ currents. Pipette solution contained (130 mM CsCl/20 mM TEACl/2 mM $MgCl_2$/5 mM ATP-2Na/10 mM Hepes/10 mM EGTA, pH 7.25), supplemented with amphotericin B. To achieve patch perforation, we front-filled patch pipettes by dipping them into the internal solution, and back-filled with the internal solution containing amphotericin B. Adequate series resistances (less than five-fold of the pipette resistances) were usually attained within 10 min after the gigaohm seal formation. Each current component was determined in each single cell by subtracting the traces after application of channel blocker. Our rapid perfusion system enables us to exchange the bath solution almost immediately, which minimizes the risk of contamination of time-dependent leak currents.

After achieving membrane perforation, the Tyrode's solution was replaced by a Na^+-free K^+-free solution (135 mM TEACl/5.4 mM CsCl/2 mM $CaCl_2$/0.53 mM $MgCl_2$/11 mM glucose, 5 mM Hepes, pH 7.4). TTX at 10 μM was added to the solution to abolish contamination with low-threshold activating TTX-sensitive Ca^{2+} currents (Vassort *et al.* 2006). According to a comparison of current-voltage (*I–V*) relationships from −100 mV and −50 mV, $I_{Ca,T}$ currents were elicited by 150 ms test pulses to −30 mV (V_H of −100 mV, 0.1 Hz). The obtained inward currents were completely blocked with 0.5 mM $NiCl_2$ (data not shown), representing most of the $I_{Ca,T}$ component. Two representative data points were referred to for optimization of the model.

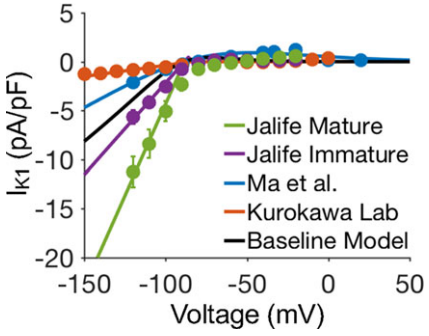

Figure 9. Inward rectifier potassium current (I_{K1}) model optimization
I–V curves for I_{K1} with dataset-specific model fits (lines) optimized to experimental data (points). The I_{K1} model used in baseline cellular model is shown in black. Coloured symbols represent experimental iPSC-CM data from Ma *et al.* (2011), the Kurokawa lab (Li *et al.* 2017) and immature and mature cell preparations from the Jalife lab (Herron *et al.* 2016).

Results

We set out to develop a computational model that can recapitulate the varied electrophysiological responses of iPSC-CMs. A schematic of the model cell containing all the ionic processes and compartments in the model is shown in Fig. 1. The process for determining all ionic current models is described by the flow chart in Fig. 2. All major ionic currents (indicated by red stars in Fig. 1) were formulated and parameterized to fit iPSC-CM experimental kinetic data, as detailed in Table 1.

Sodium current (I_{Na})

The sodium current model contains three Hodgkin–Huxley type gating variables: activation (m), fast-inactivation (h) and slow-inactivation (j), as described previously (Beeler & Reuter, 1977). The model formulation for the sodium current is shown as the example current in Fig. 1. For each gating variable, experimental data from iPSC-CMs were used to optimize model parameters (x_{1-5}). Three distinct dataset-specific models of the sodium current were optimized, based on three independent experimental datasets. One sodium dataset was from Ma *et al.* (2011) and two independent datasets were from the Jalife Lab (Herron *et al.* 2016).

The immature dataset from the Jalife Lab was collected in iPSC-CMs plated on glass coverslips (conventional cell preparation). The mature dataset from the Jalife Lab was collected in iPSC-CMs plated on polydimethylsiloxane (PDMS) coverslips, which were shown to promote mature electrophysiological function in iPSC-CMs (Herron *et al.* 2016). The Jalife Lab data were collected at room temperature. Before optimizing the model parameters, the Jalife Lab experimental data were converted to physiological temperature using $Q_{10} = 2.79$ for time constants (ten Tusscher *et al.* 2004) and $Q_{10} = 1.5$ for conductance (Correa *et al.* 1991). Experimental data shown in Fig. 3*C–D* comprise adjusted data with respect to physiological temperature. Experimental iPSC-CM voltage dependence of steady-state inactivation and activation data were used to optimized parameters for $h_\infty * j_\infty$ and ${m_\infty}^3$, respectively. The experimental data used for parameterization, as well as the resulting models, are shown in Fig. 3*A*.

Several experimentally published datasets from iPSC-CMs do not contain explicit information for the time constants of gating processes. However, current recording traces were published. To extract time constants of gating kinetics, normalized current recordings from published data were fit to single-exponential functions ($e^{-t/\tau}$; t = time, τ = time constant) for activation and/or inactivation at each voltage step. These extracted time constant values were used to optimize model parameters. In the sodium current, this technique was used to extract activation and fast-inactivation time constants from sodium current recordings in Ma *et al.* (2011) and Herron *et al.* (2016). The resulting time constant values (corrected to physiological temperature) and respective model fits are shown in Fig. 3*C* and *D*. All three dataset-specific models were optimized to data from the Kurokawa Lab for time constants of slow-inactivation, as shown in Fig. 3*E*. The maximal conductance for each model was tuned to fit the *I–V* relationship for the corresponding dataset, as shown in Fig. 3*B*. The sodium current kinetics in the baseline iPSC-CM model are shown in black (Fig. 3).

L-type calcium current (I_{CaL})

The model L-type calcium current contains voltage-dependent activation and inactivation gating variables (x_{act}, x_{inact}). Both gates were modelled using the formulation shown for example gate x in Fig. 1. The model also includes a calcium-dependent inactivation gate ($x_{inact,Ca}$) from the ten Tusccher 2004 model. The

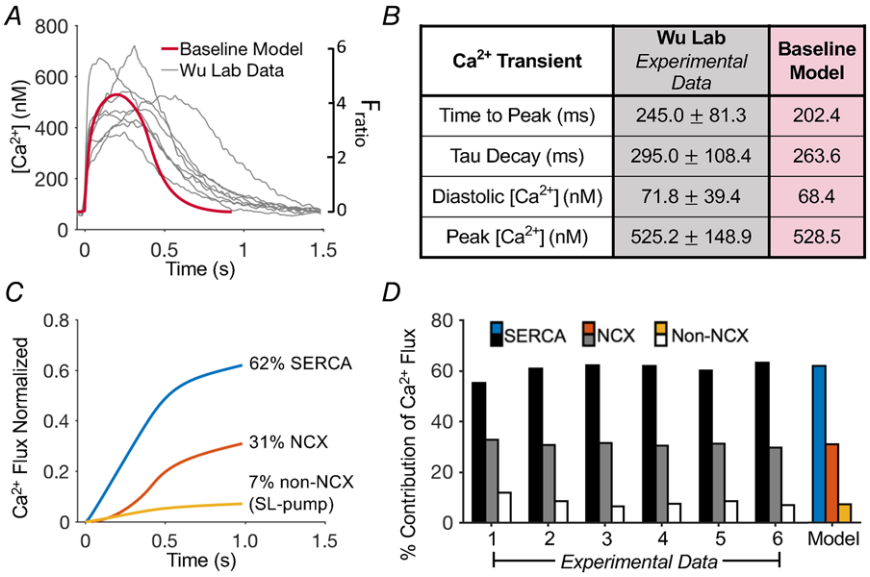

Figure 10. Optimization of calcium handling in the iPSC-CM baseline model
A, experimental iPSC-CM CaT traces from the Wu lab (grey) (Garg *et al.* 2018) with baseline model CaT (red). Experimental data were reported as the normalized Ca^{2+} florescence (F_{ratio}). Separately, average iPSC-CM peak and diastolic Ca^{2+} concentrations were measured by the Wu lab. The two *y*-axes are plotted so that the average F_{ratio} peak and diastolic values of the experimental dataset shown correspond to the average experimental concentration of peak and diastolic Ca^{2+} (*B*). The baseline model CaT output is nM. *B*, comparison of baseline model CaT morphology markers with experimental iPSC-CM data from the Wu lab. *C*, relative contribution of calcium from I_{SERCA}, I_{NCX} and I_{PMCA} to the CaT during a single AP in the baseline model. *D*, comparison of experimental (black and white) and baseline model (coloured) relative contribution of calcium flux from I_{SERCA}, I_{NCX} and I_{PMCA} during the CaT. Experimental data from Hwang *et al.* (2015).

Table 2. Details for experimental action potential datasets

Reference	Cell-line	$n =$	Cell-type
Wu Lab (A) (Garg *et al.* 2018)	IHC	14	Ventricular-like
Wu Lab (B) (Garg *et al.* 2018)	IHC	12	Ventricular-like
Herron *et al.* (2016) (PDMS – Mature)	iCell	24	Mixed morphologies
Herron *et al.* (2016) (Glass – Immature)	iCell	37	Mixed morphologies
Ma *et al.* (2011)	iCell	32	Ventricular-like
Doss *et al.* (2012) (Group A)	iCell	63	Ventricular-like
Doss *et al.* (2012) (Group B)	iCell	23	Ventricular-like
Cordeiro *et al.* (2013)	iCell	149	Mixed morphologies
Es-Salah-Lamoureux *et al.* (2016)	IHC	9	Ventricular-like
Ma *et al.* (2015)	IHC	17	Ventricular-like

*IHC, in-house control cell-line.

model L-type calcium current is described by:

$$I_{\mathrm{CaL,y}} = p_{\mathrm{CaL,y}} * x_{\mathrm{act}} * x_{\mathrm{inact}} * x_{\mathrm{inact,Ca}} * z_{\mathrm{y}}^2 * \frac{VF^2}{RT}\gamma_{\mathrm{y}}\frac{[Y]_{\mathrm{i}}e^{z_{\mathrm{y}}\mathrm{VF/RT}} - [Y]_o}{e^{z_{\mathrm{y}}\mathrm{VF/RT}} - 1} \quad (11)$$

where y is Ca^{2+}, Na^+ or K^+, $p_{\mathrm{CaL,y}}$ indicates the permeability to ion y, R is the gas constant, z_{y} is the valence of ion y, and γ_{y} is to activity coefficient for ion y as in the Shannon–Bers model. The total current is the sum of the Ca^{2+}, Na^+ and K^+ currents.

$$I_{\mathrm{CaL}} = I_{\mathrm{CaL,Ca}} + I_{\mathrm{CaL}}, \mathrm{Na} + I_{\mathrm{CaL}}, \mathrm{K} \quad (12)$$

Parameters for the voltage-dependent inactivation and activation gates (x_{inact} and x_{act}) were optimized to iPSC-CM experimental steady-state inactivation and activation curves, as well as voltage-dependent time constants of inactivation and activation. The four dataset-specific models were optimized to experimental data from Ma *et al.* (2011), Es-Salah-Lamoureux *et al.* (2016) and two independent datasets from Veerman *et al.* (2016). Es-Salah-Lamoureux *et al.* (2016) and Veerman *et al.* (2016) used an in-house iPSC-CM line for experimental results shown. I_{CaL} recordings by Ma *et al.* (2011) and Es-Salah-Lamoureux *et al.* (2016) were

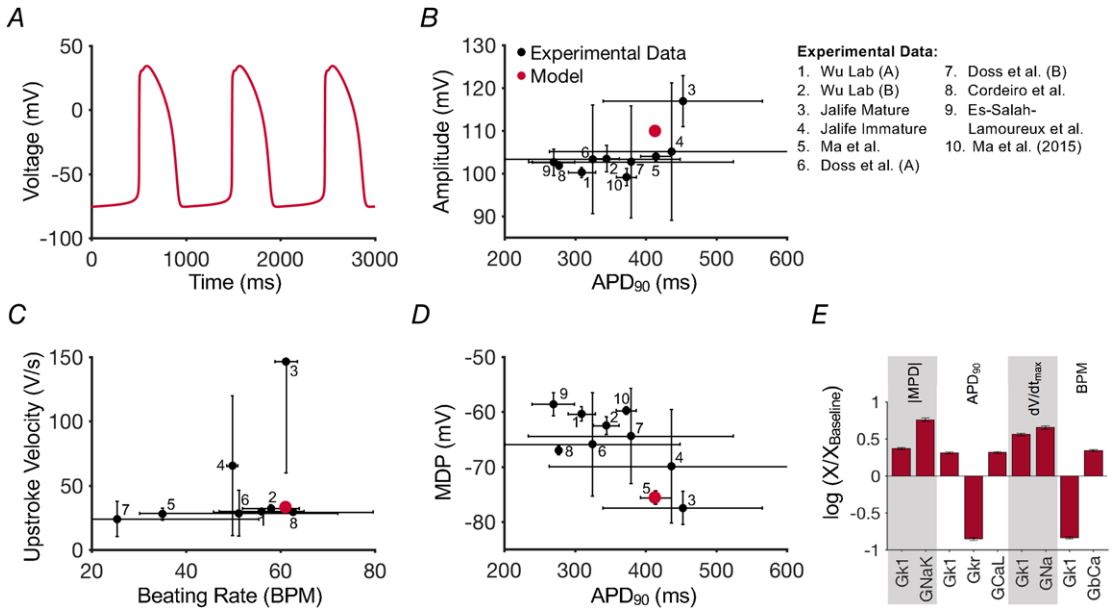

Figure 11. Characterization of the baseline model AP
A, time course of the spontaneously beating APs in the baseline model. *B–D*, comparison of AP morphology in the baseline model (red) and experimental iPSC-CM data (black). Experimental data from the Wu Lab (Garg *et al.* 2018), the Jalife Lab (Herron *et al.* 2016), Ma *et al.* (2011), Doss *et al.* (2012), Cordeiro *et al.* (2013), Es-Salah-Lamoureux *et al.* (2016) and Ma *et al.* (2015). *E*, sensitivity analysis using multivariable regression in the baseline model. Only parameters with regression coefficients >0.3 are shown.

Table 3. Model parameter details for pumps, exchangers, and SR currents

Parameter	Value	Units	Definition
k_{NCX}	1100	pA pF^{-1}	Maximal I_{NCX}
γ	0.7	–	Voltage-dependence parameter (I_{NCX})
K_{mCa}	1.38	mM	Ca_i half-saturation parameter (I_{NCX})
K_{mNa}	87.5	mM	Na_i half-saturation parameter (I_{NCX})
k_{sat}	0.1	–	Saturation factor (I_{NCX})
α	2.75	–	Outward enhancing factor (I_{NCX})
P_{NaK}	2.48	pA pF^{-1}	Maximal I_{NaK}
K_{mK}	1.0	mM	K_o half-saturation parameter (I_{NaK})
K_{mNa}	40.0	mM	Na_i half-saturation parameter (I_{NaK})
g_{PMCA}	0.2625	nS pF^{-1}	Maximal I_{PMCA} conductance
K_{PMCA}	0.0005	mM	Ca_i half-saturation parameter (I_{PMCA})
k_s	12.5	ms^{-1}	SR release rate constant (I_{Rel})
k_{oCa}	643 750	mM^{-2} ms^{-1}	Non-SR-dependent transition rate constant (J_{Rel})
k_{om}	0.2143	ms^{-1}	J_{Rel} rate constant
k_{iCa}	18.495	mM^{-1} ms^{-1}	Non-SR-dependent transition rate constant (J_{Rel})
k_{im}	0.00056	ms^{-1}	J_{Rel} rate constant
$EC_{50\text{-}SR}$	0.45	–	Parameters for $[Ca]_{SR}$-dependent activation of SR release (J_{Rel})
Max_{SR}	15	–	
Min_{SR}	1	–	
k_{CaSR}	$Max_{SR} - \frac{(Max_{SR}-Min_{SR})}{1+(\frac{EC_{50-SR}}{[Ca]_{SR}})^{2.5}}$		$[Ca]_{SR}$-dependent RyR activation coefficient (J_{Rel})
k_{oSRCa}	$\frac{k_{oCa}}{k_{CaSR}}$		J_{Rel} rate constant
k_{iSRCa}	$k_{iCa} * k_{CaSR}$		J_{Rel} rate constant
$V_{max,up}$	1.105×10^{-4}	mM ms^{-1}	Maximal J_{up}
K_{up}	1.755×10^{-4}	mM	Half-saturation constant
V_{leak}	1.6×10^{-6}	ms^{-1}	Maximal J_{leak}

conducted at room temperature and converted to physiological temperature using $Q_{10} = 2.1$ for time constants (ten Tusscher *et al.* 2004) and $Q_{10} = 2.3$ for conductance (Kiyosue *et al.* 1993).

Steady-state inactivation and activation iPSC-CM experimental data, as well as optimized dataset-specific models for each dataset, are shown in Fig. 4*A*. As a result of a lack of explicitly reported experimental iPSC-CM data for the time constants of voltage-dependent L-type calcium gating, time constants were extracted from current recordings by Ma *et al.* (2011) (as described above for the sodium current). The time constants in Ma *et al.* (2011), corrected to physiological temperature, were used to optimize all models. The experimental conditions for calcium buffering during the I_{CaL} current recordings by Ma *et al.* (2011) (5 mM EGTA), may result in some calcium-dependent inactivation contribution to the time constants of inactivation derived from these current recordings. Because this calcium-dependent inactivation contribution was not quantified experimentally, the time constants of inactivation derived from the current recordings were assumed to be entirely voltage-dependent inactivation for model parameterization. The time constant data used for model optimization, and the resulting models, are shown in Fig. 4*C* and *D*.

The calcium-dependent inactivation gate ($x_{inact,Ca}$) formulation in the ten Tusscher 2004 model was retained in this model as a result of a lack of experimental data characterizing calcium-dependent inactivation in iPSC-CMs. A single scaling factor for $[Ca]_i$ in $x_{inact,Ca,\infty}$ was optimized in the final whole-cell parameter optimization to recapitulate iPSC-CM calcium handling. This was required to accommodate the lower $[Ca]_i$ throughout the iPSC-CM AP compared to the adult ventricular cell model in the ten Tusscher 2004 model. Figure 4 shows all of the I_{CaL} models with the final optimized calcium-dependent inactivation gate.

Values for γ_{Ca}, γ_{Na} and γ_K, and the relative proportions of $p_{CaL,Ca}$:$p_{CaL,Na}$:$p_{CaL,K}$ were retained from the Shannon–Bers model (Shannon *et al.* 2004). The total permeability ($p_{CaL} = p_{CaL,Ca} + p_{CaL,Na} + p_{CaL,K}$) of each dataset-specific model was tuned using the experimental *I–V* curves and the resulting *I–V* relationships are shown in Fig. 4*B*. The baseline model for I_{CaL} is shown in black in Fig. 4.

T-type calcium current (I_{CaT})

The T-type calcium current was introduced to the iPSC-CM model because it is experimentally found

in iPSC-CMs. T-type calcium is typically found in embryonic hearts and its expression is dependent on the developmental stage of the heart (Ono & Iijima, 2010). T-type calcium is also found experimentally in iPSC-CMs (Ivashchenko *et al.* 2013; Karakikes *et al.* 2015), as is expected as a result of the iPSC-CMs immature cardiac phenotype. The T-type calcium current was modelled as in the previously published sinoatrial node model by Maltsev & Lakatta (2009). Peak I_{CaT} was tuned to the *I–V* curves for I_{CaT} provided by the Kurokawa Lab, as shown in Fig. 4*E*.

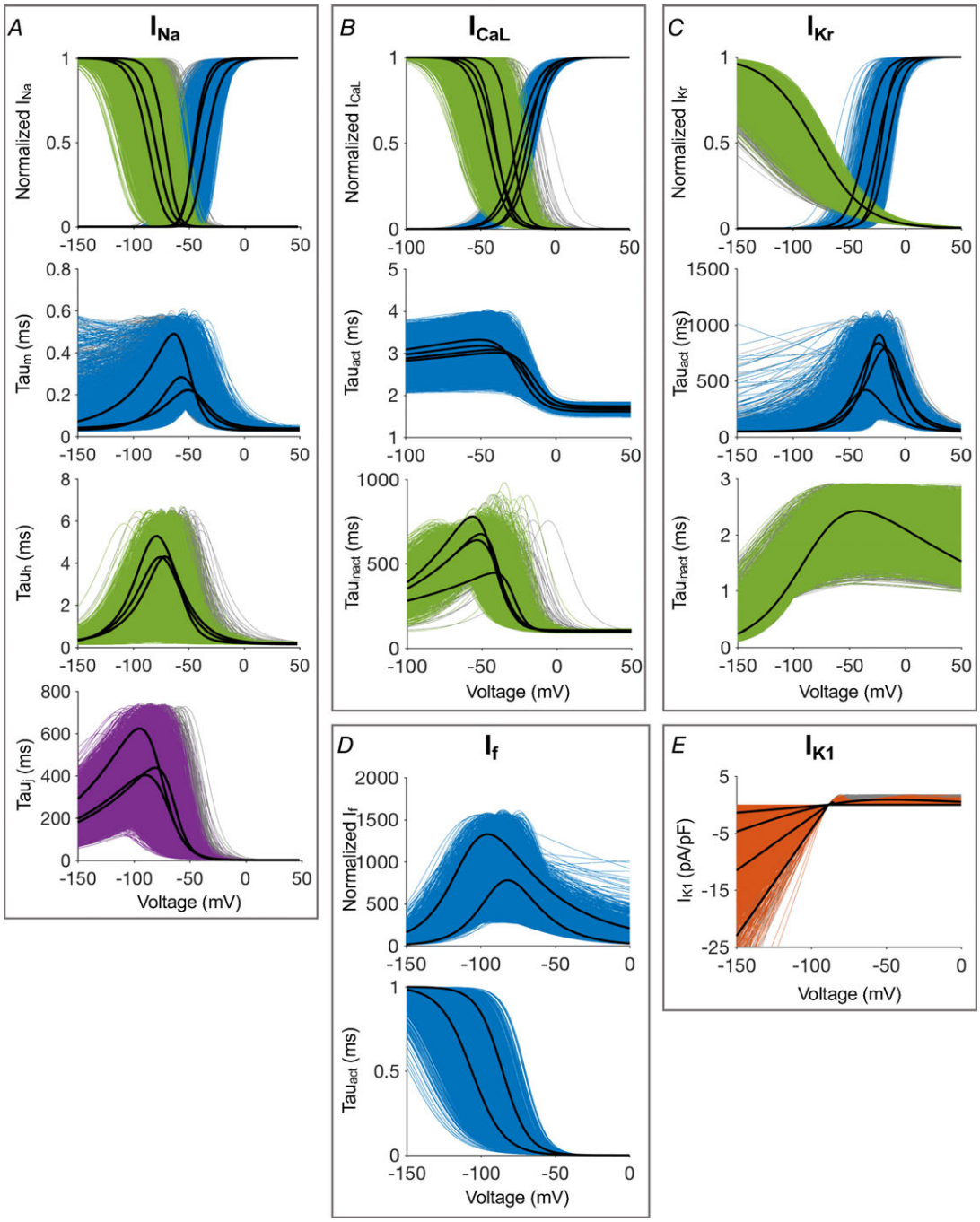

Figure 12. Kinetic variability generated by varying individual current model parameters
Steady-state and time constant curves for each gate in (*A*) I_{Na}, (*B*) I_{CaL}, (*C*) I_{Kr} and (*D*) I_f. *E*, *I–V* curves for I_{K1}. Dataset-specific model fits (black lines, also shown in Figs 3–10), randomly-parameterized models resulting in spontaneous AP generation in the cell models (coloured lines) and randomly-parameterized models resulting in non-spontaneous or non-AP generating model cells (grey lines) are all shown.

Rapid delayed rectifier potassium current (I_{Kr})

The rapid delayed rectifier potassium current was modelled as:

$$I_{Kr} = g_{Kr} * \sqrt{\frac{K_0}{5.4}} * x_{act} * x_{inact} * (V_m - E_K) \quad (13)$$

The voltage-dependent activation and inactivation gating variables (x_{act}, x_{inact}) were modelled using the formulation shown for the exemplar gate x in Fig. 1. The K_o dependence of the current ($\sqrt{K_o/5.4}$) and the voltage-dependent inactivation gate was retained from the ten Tusscher 2004 formulation of I_{Kr}. To utilize the simplified gating model formulation for the I_{Kr} inactivation gate (x_{inact}), the single-exponential voltage-dependent rate constant model (Fig. 1, right) was optimized to fit the voltage-dependence of I_{Kr} inactivation in the ten Tusscher 2004 model. The resulting model of inactivation gating is shown in Fig. 5*A* and *D*.

Dataset-specific models of steady-state activation were fit to four independent iPSC-CM experimental datasets from the Wu Lab (Garg *et al.* 2018), as well as from Ma *et al.* (2011), Bellin *et al.* (2013) and Es-Salah-Lamoureux *et al.* (2016). The data by Es-Salah-Lamoureux *et al.* (2016) were collected from an in-house iPSC-CM line and the data by Bellin *et al.* (2013) were collected from a patient-specific cell line. Voltage-dependent time constants of activation

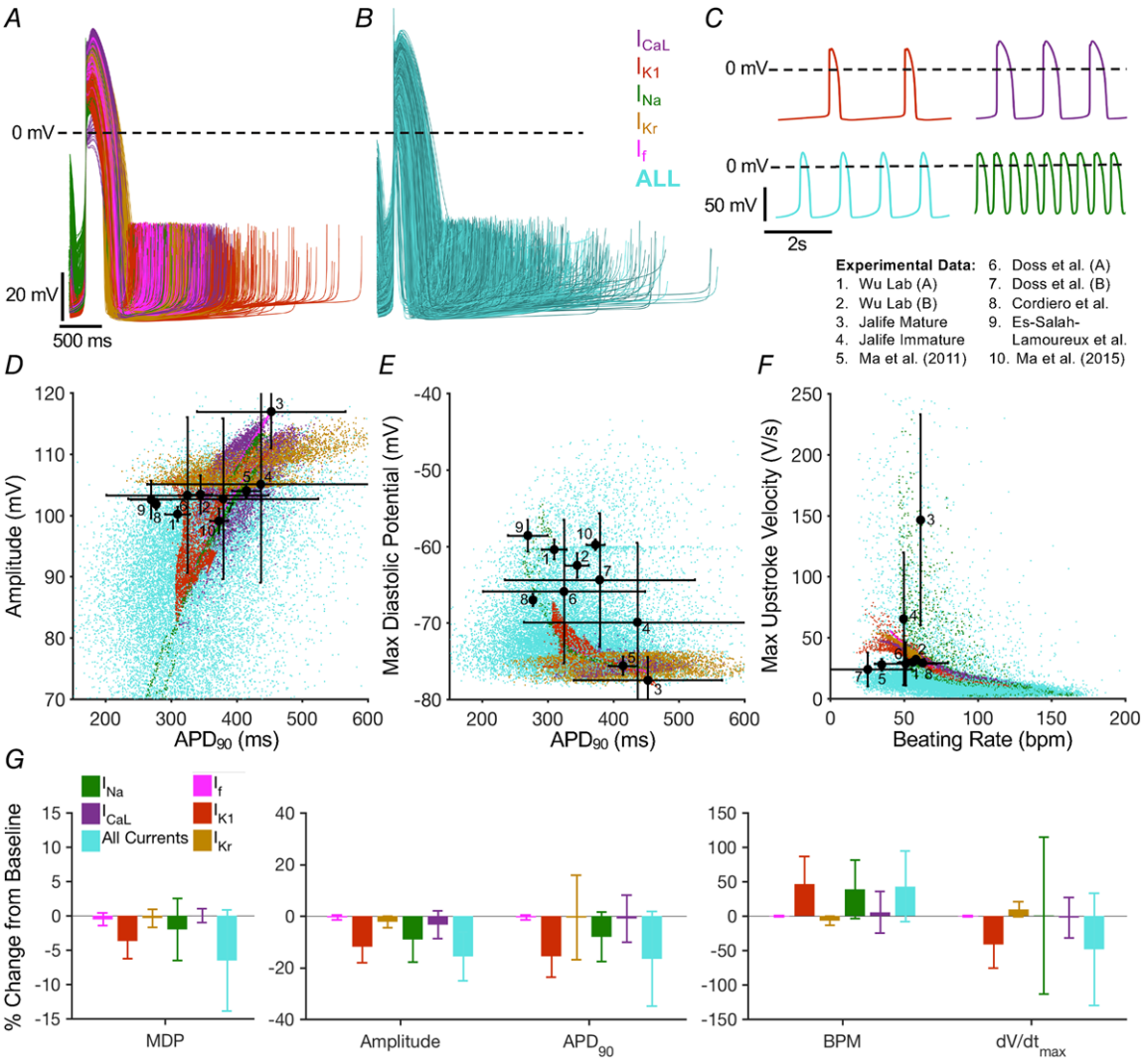

Figure 13. Variation of action potential morphology in model iPSC-CM populations
A, APs of spontaneously beating cells (n = 25,434) generated by varying one current at a time (I_{Na}, I_{CaL}, I_{Kr}, I_f and I_{K1}). *B*, APs of spontaneously beating cells (n = 17,139) generated by varying the same five currents simultaneously. *C*, representative AP time courses of spontaneously beating cells at various pacing frequencies. *D–F*, comparison of AP morphology in the populations of models (colour) and experimental iPSC-CM data (black). Each coloured point represents a spontaneously beating cell created by varying a single current (*A*), or by varying all five currents simultaneously (*B*). *G*, mean ± SD of AP morphology measures for each population, normalized to the baseline model AP.

were extracted from current recordings published in Ma *et al.* (2011). The time constants of activation in Ma *et al.* (2011) were used to optimize parameters in the optimized models of Ma *et al.* (2011), the Wu Lab (Garg *et al.* 2018) and Es-Salah-Lamoureux *et al.* (2016). Experimental time constants of activation were published in Bellin *et al.* (2013) and used in the corresponding model, as shown in green in Fig. 5*C*. Finally, the maximal conductance (g_{Kr}) of each dataset-specific model was tuned to the *I–V* relationship data for each dataset, shown in Fig. 5*B*. Bellin *et al.* (2013) published a single data point for the experimental *I–V* relationship (at $V_m = 60$ mV, not shown), which was used to optimize the maximal conductance of the corresponding model.

Transient outward potassium current (I_{to})

The transient outward potassium current was modelled as:

$$I_{to} = g_{to} * x_{act} * x_{inact} * (V_m - E_K) \quad (14)$$

The voltage-dependent activation and inactivation gating variables (x_{act}, x_{inact}) were modelled using the formulation of example gate *x* in Fig. 1. iPSC-CM experimental data from Ma *et al.* (2011), Cordeiro *et al.* (2013) and Veerman *et al.* (2016) were used to optimize dataset-specific models. Experimental results in Veerman *et al.* (2016) were recorded in an in-house iPSC-CM cell-line. Steady-state activation and time constants of inactivation were extrapolated from I_{to} current recordings published in Ma *et al.* (2011). Time constants of inactivation from Ma *et al.* (2011) were used to optimize the inactivation time constant parameters of the model by Veerman *et al.* (2016). Steady-state activation data from Ma *et al.* (2011) were used to optimize the model of Cordeiro *et al.* (2013) and steady-state inactivation data from Cordeiro *et al.* (2013) were used to optimize the model of Ma *et al.* (2011) because neither dataset included both steady-state activation and inactivation data.

Time constants for activation of I_{to} were not available in iPSC-CMs; thus, model parameters were optimized to retain the ten Tusscher 2004 voltage-dependence for time constants of activation. The resulting model for time constants of I_{to} activation are shown in Fig. 6*C*. Finally, maximal conductance (g_{to}) was tuned to experimental iPSC-CM *I–V* relationships for each dataset, as shown in Fig. 6*B*.

Slow delayed rectifier potassium current (I_{Ks})

The slow delayed rectifier potassium current was modelled as:

$$I_{Ks} = g_{Ks} * x_{act}^2 * (V_m - E_K) \quad (15)$$

The voltage-dependent activation gating variable (x_{act}) was modelled using the formulation of example gate *x* in Fig. 1. Dataset-specific models were optimized to experimental data from Ma *et al.* (2011) and two independent datasets from Ma *et al.* (2015), shown in Fig. 7*A* (Ma *et al.* 2011; Ma *et al.* 2015). Ma *et al.*

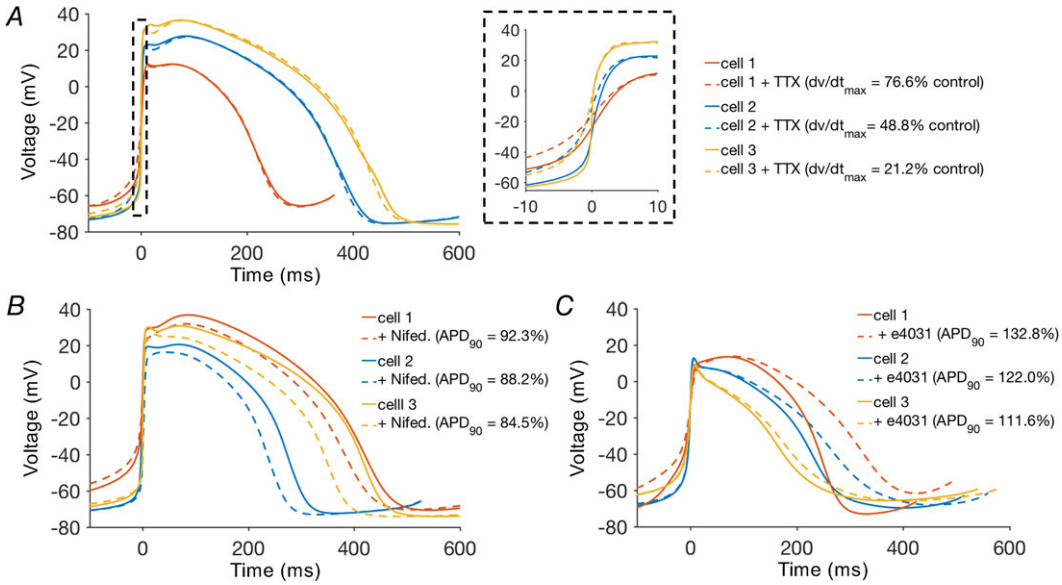

Figure 14. Sample APs showing the effect of ion channel blockers within the model population
Showing the same cellular models in the control (solid lines) and drugged (dashed lines) conditions. Three cells are shown for each drug, representing a cell with a change in the given AP parameter near the population mean (cell 2) (± 1 SD). The mean ± SD for the full population are described in Table 4. Drug effects are shown for (*A*) TTX, (*B*) nifedipine and (*C*) E-4031.

(2015) recorded one I_{Ks} dataset in a patient-specific iPSC-CM cell-line, and another dataset in iCell iPSC-CMs. Parameters for $x^2_{act,\infty}$ were optimized to steady-state activation data, as shown in Fig. 7*A*. As a result of a lack of available experimental data for the time constants of I_{Ks} activation, time constants extracted from current recordings published in Ma *et al.* (2011) were used to optimize parameters in all models, as shown in Fig. 7*B*. Finally, the maximal conductance (g_{Ks}) was tuned to *I–V* data, as shown in Fig. 7*C*. For both models built on datasets of Ma *et al.* (2015) (Fig. 7, patient-specific in orange, iCell in purple), the maximal conductance was tuned to the *I–V* relationship in iCells of Ma *et al.* (2015), as shown by purple points in Fig. 7*C*.

Pacemaker/funny current (I_f)

The pacemaker current was incorporated into the iPSC-CM model, as it is experimentally found in iPSC-CMs (Karakikes *et al.* 2015; Kim *et al.* 2015). The current was formulated as:

$$I_f = g_F * x_{act} * (V_m - E_f) \quad (16)$$

where E_f and g_f are calculated as a balance of the sodium and potassium Nernst potentials (Verkerk & Wilders, 2013), such that:

$$g_f(V_m - E_f) = g_{f,Na}(V_m - E_{Na}) + g_{f,K}(V_m - E_K) \quad (17)$$

where the ratio of $g_{f,Na}$:$g_{f,K} = 0.491$, based on prior models of I_f in rabbit sinoatrial node (Verkerk & Wilders, 2013). The activation gate (x_{act}) is modelled using the same formulation as example gate x in Fig. 1. Experimental data in iPSC-CMs from Ma *et al.* (2011) and the Kurokawa Lab (Li *et al.* 2017) were used to optimize dataset-specific models. Model parameters for the activation gate (x_{act}) were optimized to experimental data for steady-state activation and time constants of activation, as shown in Fig. 8*A* and *B*. Maximal conductances (g_f) for each dataset-specific model were fit to *I–V* relationships of the corresponding experimental dataset. The experimental data and resulting models are shown in Fig. 8*C*.

Inward rectifier potassium current (I_{K1})

The slow delayed rectifier potassium current was modelled as:

$$I_{K1} = g_{K1}\sqrt{\frac{K_0}{5.4}} * x_{act,\infty} * (V_m - E_K) \quad (18)$$

The K_o dependence of the current ($\sqrt{K_o/5.4}$) is retained from the ten Tusscher 2004 formulation of I_{K1}. To recapitulate the behaviour of I_{K1}, the activation gate was formulated as:

$$\alpha_x = x_1 e^{(V+x_3)/x_2} \quad (19)$$

$$\beta_x = e^{(V+x_5)/x_4} \quad (20)$$

Dataset-specific models were created by optimizing parameters x_{1-5} and g_{K1} to the *I–V* relationships recorded in iPSC-CMs from Ma *et al.* (2011), the Kurokawa Lab (Li *et al.* 2017) and the Jalife Lab (Herron *et al.* 2016). Experimental data from the Jalife Lab were collected at room temperature. The Jalife Lab *I–V* curves were corrected to physiological temperature using $Q_{10} = 1.5$ (Kiyosue *et al.* 1993). The experimental data used to optimize the models, and the resulting models are shown in Fig. 9.

Pump and exchanger currents (I_{NCX}, I_{NaK}, I_{PMCA})

To model the remaining membrane currents which are not characterized in iPSC-CMs, we utilized previous models. The sodium-calcium exchanger (I_{NCX}), sodium potassium pump (I_{NaK}) and sarcolemma pump (I_{PMCA}) currents were modelled using formulations from prior ventricular cell models (Luo & Rudy, 1994; ten Tusscher *et al.* 2004). Kinetics of these currents were retained from existing ventricular cell models because these currents have not been characterized experimentally in iPSC-CMs. Maximal values of all three currents were included in the whole-cell optimization routine (Fig. 2, step 2) and the final parameterizations are detailed in Table 3.

$$I_{NCX} = k_{NCX} * \frac{\left(e^{\gamma VF/RT} * [Na]_i^3 * [Ca]_o\right) - \left(e^{\frac{(\gamma-1)VF}{RT}} * [Na]_o^3 * [Ca]_i * \alpha\right)}{\left(K_{mNa}^3 + [Na]_o^3\right) * (K_{mCa} + [Ca]_o) * \left(1 + k_{sat} * e^{\frac{(\gamma-1)VF}{RT}}\right)} \quad (21)$$

$$I_{NaK} = \frac{P_{NaK} * [K]_o * [Na]_i}{([K]_o + K_{mK}) * ([Na]_i + K_{mNa}) * (1 + 0.1245 * e^{\frac{-0.1*VF}{RT}} + 0.0353 * e^{\frac{-VF}{RT}})} \quad (22)$$

$$I_{PMCA} = g_{PMCA} * \frac{[Ca]_i}{([Ca]_i + K_{PMCA})} \quad (23)$$

SR currents (J_{Rel}, J_{up}, J_{leak})

The calcium handling in iPSC-CMs has not been fully characterized experimentally. Thus, the calcium handling in the present model is based on prior formulations of SR currents. Parameters for the RYR (J_{rel}) were adapted from the Shannon–Bers model to maintain physiological SR function during the beating cycle. The Shannon–Bers RYR formulation is dependent on the high calcium concentration in the cleft compartment described in the Shannon–Bers cellular geometry. However, the geometry used in the present model does not include

this cleft compartment (as shown schematically in Fig. 1). Given these differences in cellular geometry, the original Shannon–Bers J_{Rel} parameters do not produced a SR release during the AP in the simplified cellular geometry used in this model. To implement the Shannon–Bers RYR Markov model formulation within the cellular geometry described above, RYR transition rates were determined by our whole-cell optimization routine (Fig. 2, Step 2). Maximal values of J_{up} and J_{leak} were also included in the whole-cell optimization. Final parameterizations of all SR currents are detailed in Table 3.

$$J_{up} = \frac{V_{max,up}}{\left(1 + \frac{K_{up}{}^2}{[Ca]_i{}^2}\right)} \tag{24}$$

$$J_{leak} = V_{leak} * ([Ca]_{SR} - [Ca]_i) \tag{25}$$

For closed (C), open (O), inactivated (I) and closed-inactivated (CI) states of J_{Rel}:

$$CI = 1 - C - O - I \tag{26}$$

$$\frac{dC}{dt} = (k_{im} * CI - k_{iSRCa} * [Ca]_i * C) - \left(k_{oSRCa} * [Ca]_i{}^2 * C - k_{om} * O\right) \tag{27}$$

$$\frac{dO}{dt} = \left(k_{oSRCa} * [Ca]_i{}^2 * C - k_{om} * O\right) - (k_{iSRCa} * [Ca]_i * O - k_{im} * I) \tag{28}$$

$$\frac{dI}{dt} = (k_{iSRCa} * [Ca]_i * O - k_{im} * I) - \left(k_{om} * I - k_{oSRCa} * [Ca]_i{}^2 * CI\right) \tag{29}$$

$$J_{Rel} = k_s * O * ([Ca]_{SR} - [Ca]_i) * \frac{V_{SR}}{V_C} \tag{30}$$

Model development: intracellular Ca^{2+} dynamics

Figure 10*A* shows the baseline model (red) calcium transient compared to experimental CaTs from the Wu Lab (grey). Experimental CaTs shown are reported as a florescence ratio (F_{ratio}), as plotted in Fig. 10*A* on the right *y*-axis. The average peak F_{ratio} value of the dataset shown (Peak $F_{ratio} = 4.25$) corresponds to the independently measured iPSC-CM average peak CaT concentration (Fig. 10*B*) on the left *y*-axis. Similarly, the diastolic F_{ratio} value (Diastolic $F_{ratio} = 0$) also corresponds to the independently measured iPSC-CM average diastolic CaT concentration (Fig. 10*B*).

To reproduce the CaT data described above, SR currents (J_{Up}, J_{Rel} and J_{leak}) and calcium-dependent transmembrane currents that were not previously parameterized to fit iPSC-CM data (I_{NCX}, I_{PMCA}) were optimized to recapitulate the experimentally observed iPSC-CM CaT morphology shown in Fig. 10*B*. The baseline model parameters were optimized to produce CaT outputs within 1 SD of the experimental Ca^{2+} transient markers shown. Additionally, the optimization considered the ratio of time to peak and time constant of decay of the CaT. The baseline model has a faster spontaneous beating rate (62.0 beats min^{-1}) than the average spontaneous beating rate in the CaT dataset from the Wu Lab (30.2 $\pm$ 13.2 beats min^{-1}). To normalize the experimental data and account for this difference in pacing rate, we included the ratio of the CaT time to peak and CaT time constant of decay as a target in our optimization error function. The ratio of the time to peak and time constant of decay of the experimental CaT was 0.83, and the resulting baseline model CaT ratio is 0.77. Thus, the model recapitulates the relative portion a single AP cycle spent at each phase of the CaT.

The model was also tuned to recapitulate the relative contribution of three fluxes (I_{NCX}, J_{Up} and I_{PMCA}) to the calcium removal pathways (Fig. 10*C* and *D*) (Hwang *et al.* 2015). Experimentally, the contribution of NCX (I_{NCX}), SERCA (J_{Up}) and the sarcolemma pump (I_{PMCA}) is calculated using the time constant of the CaT during a normal AP, the caffeine-induced CaT and the caffeine-induced CaT in a sodium and calcium-free solution (Bers, 2000). Hwang *et al.* (2015) provided a comparison of the relative contributions I_{NCX}, J_{Up} and I_{PMCA} to the calcium flux balance from six independent iPSC- CM datasets across three laboratories. Maximal I_{NCX}, J_{Up} and I_{PMCA} in the baseline model were optimized to fit the relative contributions of each current. The relative contribution to the calcium flux in the model was calculated based on the integral of each current during a single CaT. This integral, normalized to total calcium contribution from all three sources, is shown in Fig. 10*C* for a single beat in the baseline model, obtained after achieving steady-state. The resulting relative contributions to calcium flux pathways in the model are comparable to the experimentally observed ranges (Fig. 10*D*).

Model prediction: whole cell simulations

The baseline model that was developed via the steps described above recapitulates the phenotype of typical iPSC-CMs (Fig. 11*A*). The AP and CaT outputs fall within the experimental range of behaviours (Figs 10 and 11). Experimental details of the AP datasets used are described in Table 2. The baseline model was optimized to reproduce these key features of the immature iPSC-CM phenotype, including spontaneous beating (Fig. 11*A* and *C*), a reduced AP amplitude (Fig. 11*B*), a low maximal upstroke velocity (Fig. 11*C*) and a depolarized maximum diastolic

potential (MDP) (Fig. 11*D*). For precise definitions of AP morphology markers, see the Methods. The baseline model also spontaneously beats during total I_{Na} and I_f block, showing that the mechanism of automaticity in the baseline model is consistent with the experimentally observed mechanism (Guo *et al.* 2011; Itzhaki *et al.* 2011; Sheng *et al.* 2012; Kim *et al.* 2015). Sensitivity analysis on the baseline model was conducted using a multivariable regression model (Fig. 11*E*) (Sobie, 2009). The sensitivity analysis shows several expected results for cardiac cells such as increased upstroke velocity with increased sodium current, APD shortening with increased I_{Kr} and APD lengthening with increased I_{CaL}. Additionally, increased I_{K1} is experimentally shown to hyperpolarize iPSC-CM MDP (Bett *et al.* 2013; Vaidyanathan *et al.* 2016), which is consistent with the results of this sensitivity analysis (Fig. 11*E*) showing that increased I_{K1} hyperpolarizes the cells (indicated by a positive regression coefficient for I_{K1} related to the absolute value of MDP).

Although Fig. 11*B–D* shows that the baseline model falls within the experimental range, the compilation of experimental data sources also serves to illustrate the vast range of AP behaviour in 'normal' iPSC-CMs. This range of experimentally observed behaviours reveals that a single 'average' iPSC-CM model is insufficient to describe the behaviour of iPSC-CMs, and that variability may be the defining characteristic.

Model prediction: inter-subject variability

To model heterogeneity in kinetic behaviour in healthy iPSC-CMs, a population-based approach was utilized. The goal of this approach was to harness the range of experimentally observed kinetics in each ionic current and create an *in silico* population of model cells that captured the full range of iPSC-CM kinetic behaviour.

A population of models was developed to incorporate experimentally measured kinetic variability in five of the reformulated ionic currents that were identified in the multivariable regression sensitivity analysis as most important to AP behaviour (Fig. 11*E*). The five currents were I_{Na}, I_{CaL}, I_{Kr}, I_f and I_{K1}. The regression coefficients for I_f were below the threshold for Fig. 11*E*, although I_f did impact MDP and BPM in the model but at a lower level than the other currents shown in Fig. 11*E*. I_{NaK} was identified by the sensitivity analysis but, as a result of the lack of experimental iPSC-CM data characterizing the range of kinetic behaviour in I_{NaK}, it was not included in the population-based variability.

In total, six populations were developed. In five of those populations, model parameters for a single current were varied and all the other currents were kept at the baseline values. The populations capture inter-subject variability observed in the measured electrophysiology data. In the final population, the parameters were simultaneously varied for all five of the identified currents.

To simulate model cell variability, ionic current models were randomly parameterized within the experimentally observed ranges from multiple data sets for steady-state gating, time constants of gating and *I–V* relationships. Using the mean ± SD of each parameter value across the independent dataset-specific models, a normal distribution was created for each parameter value, as described in further detail in the Methods and Fig. 2. For each model cell within the population, parameters were randomly chosen from this distribution. Thus, every model cell in the population has a unique parameter-set chosen from the normal distribution of underlying parameters composing a single current. The range of kinetic behaviours are shown for populations with single current variation in I_{Na} (Fig. 12*A*), I_{CaL} (Fig. 12*B*), I_{Kr} (Fig. 12*C*), I_f (Fig. 12*D*) and I_{K1} (Fig. 12*E*). Steady-state and time constant values functions shown in Fig. 12 are the results of random variation in the parameter values of each of the selected five currents. These randomly determined kinetics result in the whole-cell behaviour shown in Fig. 13.

A final population was built using the same methodology but by varying the kinetics of the five specified currents simultaneously (shown as effects on the AP in blue in Fig. 13). The outputs of the spontaneously beating AP models from the single-current variation populations are shown in Fig. 13*A* and the spontaneously beating AP generating models from the five-current simultaneously varied population are shown in Fig. 13*B*. Each cell in the resulting populations can be categorized into one of three groups: spontaneously beating cells, stimulated beating cells or cells excluded from analysis. 'Spontaneously beating cells' maintain automaticity with a viable AP and are most representative of the experimentally observed iPSC-CMs. The baseline model would be categorized in the spontaneous beating subpopulation. 'Stimulated beating cells' are model cells that result in a viable AP with the application of a stimulus current but are non-spontaneously beating (not shown). Cells were not analysed if they did not fully repolarize (MDP > -40 mV, AP amplitude <70 mV) or exhibited non-control/non-healthy AP morphology (e.g. alternans). Additionally, cells with non-physiological calcium handling (determined as CaT amplitude greater than 3 SDs of the experimental average in Fig. 10*B*) were excluded from the analysis.

For the cell population subject to single-current variation, only the I_{K1} variation population produced a stimulated beating subpopulation that required an external stimulus. A random selection of models from the spontaneously beating AP generating populations is shown in Fig. 13*C* to illustrate the range of beating rates and AP morphologies observed. All subsequent analyses were conducted in the subpopulation

generating spontaneously beating APs. Variation in AP morphology markers within each population of models is shown in Fig. 13*D–G*. Individual coloured points in Fig. 13*D–F* represent a single model in the given population. Additionally, these outputs are compared w2ith experimentally measured iPSC-CM outputs shown as black dots and lines (Ma *et al.* 2011; Doss *et al.* 2012; Cordeiro *et al.* 2013; Ma *et al.* 2015; Es-Salah-Lamoureux *et al.* 2016; Herron *et al.* 2016), as was performed for the baseline model in Fig. 11. It should be noted that the plots show the SE for the experimental data, meaning that the full range of experimental behaviour is larger than represented by the black points. The range of individual models in the single-current variation populations can serve as a form of sensitivity analysis: for a given morphology marker, the widest spread of models is indicative of increased sensitivity to the varied current. For example, the maximal upstroke velocity is sensitive to I_{Na} and thus the models from the I_{Na} varied population show the largest range of upstroke velocity values (Fig. 13*F*, distribution of green points along the *y*-axis). Finally, the population with simultaneous variation of five ionic currents shows the largest range of variability in all AP morphology markers and is the population most representative of the full experimentally observed space. This serves as a first step in modelling known variability of iPSC-CMs at the ionic level, resulting in the recapitulation of observed variability in iPSC-CMs at the whole-cell level.

Model prediction: ionic current block

To further validate the model population, we predicted the effect of ionic current blockers on the model population. We simulated the effect of drugs that have been experimentally studied in iPSC-CMs: TTX (I_{Na} block), E-4031 (I_{Kr} block) and nifedipine (I_{CaL} block). For each drug, we simulated a concentration that had been studied across several experimental datasets. We modelled drug effects as a simple pore block. IC_{50} values for each cell in the population were randomly selected within the range of experimentally observed IC_{50} values in stem cell-derived cardiomyocytes (Peng *et al.* 2010; Ma *et al.* 2011; Harris *et al.* 2013; Gibson *et al.* 2014; Moreau *et al.* 2017). The ranges of IC_{50} values, and corresponding percentage ionic current block, are described in Table 4. For example, when modelling 10 μM TTX, each model cell had a randomly determined IC_{50} within the experimental range, resulting in 88%–94% I_{Na} block. Beginning at the previously determined control steady-state initial conditions, each simulation was run for 200 s with drug applied, and the final AP was analysed. All simulated results shown are in spontaneously beating model cells. The percentage change in the AP parameter associated with the blocked current is described in Table 4, and sample APs for each drug are shown in Fig. 14. Only the subpopulations of models that resulted in spontaneous beating and normal repolarization after drug application were analysed. Additionally, the TTX response was only analysed in the subpopulation of model cells with more than -10 pA pF^{-1} peak I_{Na} during the control (non-drug) AP. The size and results of the analysed model subpopulations are reported in Table 4. It should be noted that the baseline model has a peak I_{Na} of -29.2 pA pF^{-1} during the AP. Models without substantial I_{Na} during the AP are unaffected by TTX and were omitted for clarity. A highly variable iPSC-CM response to TTX and other sodium channel blockers has also been observed experimentally (Sheng *et al.* 2012).

The drug-induced changes to AP morphology predicted by our model population falls within the experimentally observed range, as characterized in Table 4 (Peng *et al.* 2010; Ma *et al.* 2011; Jonsson *et al.* 2012; Gibson *et al.* 2014; Scheel *et al.* 2014; Hortigon-Vinagre *et al.* 2016). It should be noted that there is a large range of experimentally observed variation in the effects of each of these drugs. Experimental data shown in Table 4 include data from paced and spontaneously beating cells, which may contribute to this variability. However, for TTX, Jonsson *et al.* (2012) shows a similar range of change in upstroke velocity in paced and spontaneously beating cells treated with TTX. Additionally, Hortigon-Vinagre *et al.* (2016) show that cell line differences have an impact on the observed response to nifedpine and E-4031 in spontaneously beating APs. Hortigon-Vinagre *et al.* (2016) and Jonsson *et al.* (2012) reported AP outputs in spontaneously beating cells, whereas the other studies reported AP outputs at 1 Hz pacing. Qualitatively, experimental results across these experimental protocols show a similar response to each ionic channel blocking drug. Our comparison of model outputs with the experimental range reported in Table 4 serves to show that our model population can replicate this qualitative response to simple pore block.

Table 4 shows the range of the mean behaviour amongst the datasets cited, although the full range of behaviour in individual cells between these datasets is even larger. As discussed previously when characterizing the baseline AP morphology, it is impossible to pinpoint 'normal' iPSC-CM response. There is a wide range of variability in the ionic currents regulating iPSC-CM APs, and this is reflected in the range of responses to a particular drug.

Immature and mature phenotypes

We next compared representative immature and mature model phenotypes. The previously described baseline model was used as the representative immature model. The representative mature model was created using the baseline model with a 100% increase in maximal conductance of I_{K1} and a 45% increase in maximal conductance of I_{Na}.

Table 4. Simulation specifics and model population outputs for response to ionic current blockers

	TTX	Nifedipine	E-4031
Concentration	10 μM	30 nM	10 nM
Ionic current blocked	I_{Na}	I_{CaL}	I_{Kr}
Range of IC_{50} values (nM)	640–13 55[1,2]	30–39[1,3,4]	7–17[3,4,5]
% Current block	88–94%	72–77%	47–59%
Output measured	Maximum upstroke velocity	APD_{90}	APD_{90}
Experimental output w/drug (range of dataset means)	16.7–60%[1,6,7]	67.7–88.9%[1,3,4,8]	113–160%[1,3,4,8]
Output w/drug in model subpopulation	48.6 ± 27.5%	89.8 ± 5.1%	121.8 ± 10.4%
Model subpopulation (*n*)	1057	11 894	8398

1, Ma *et al.* 2011; 2, Moreau *et al.* 2017; 3, Peng *et al.* 2010; 4, Gibson *et al.* 2014; 5, Harris *et al.* 2013; 6, Scheel *et al.* 2014; 7, Jonsson *et al.* 2012; 8, Hortigon-Vinagre *et al.* 2016.

These changes represent the relative increase in I_{K1} and I_{Na} from the immature to mature phenotype, as characterized experimentally by the Jalife Lab (Figs 3*B* and 9). These increases in I_{K1} and I_{Na} are proportional to the increase in I_{K1} and I_{Na} peak current between iPSC-CMs cultured on glass (immature) and PDMS (mature) reported in Herron *et al.* (2016). The behaviour of the immature and mature models is compared in Fig. 15. The APs of the immature and mature models are shown in Fig. 15*A*, and the AP morphology markers for each model are compared with experimentally measured APs from the Jalife Lab in Fig. 15*B*. Cell outputs (experimental and computational) were normalized to the average value of the experimental iPSC-CMs cultured on PDMS (Fig. 15*B*, black). Finally a multivariable regression model, created using the same methodology as described for the baseline model (Sobie, 2009) and shown in Fig. 11*E*, was used to conduct sensitivity analysis on both the mature and baseline/immature models, and a comparison of the results is shown in Fig. 15*C*.

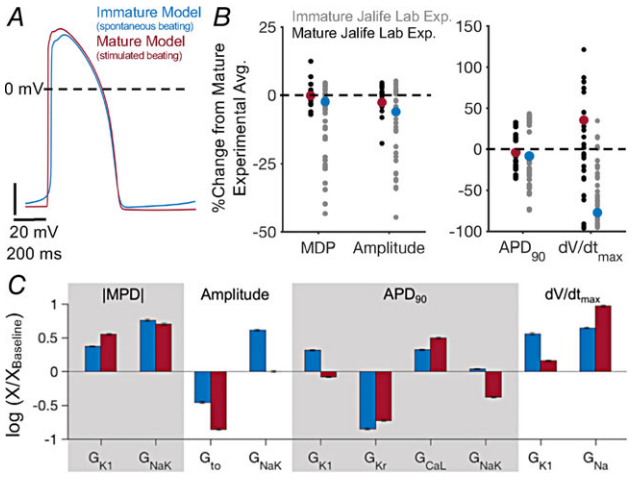

Figure 15. Comparison of immature and mature cellular models
A, AP for the immature (baseline) cellular model compared to AP for a representative mature cellular model. Immature and mature cellular models determined by scaling g_{K1} and g_{Na} based on peak currents reported in iPSC-CMs with control (immature) and maturation-promoting cell preparations (Herron *et al.* 2016). *B*, comparison of models and experimental AP morphology for mature and immature cell-types. Experimental data are from the Jalife Lab (Herron *et al.* 2016). All of the model and experimental data were normalized to the Jalife Lab mature experimental dataset average. *C*, comparison of sensitivity analysis immature and mature models using multivariable regression. Only parameters with regression coefficients >0.3 are shown.

For all four AP morphology markers (MDP, AP amplitude, APD_{90} and maximal upstroke velocity), the mature model (Fig. 15*B*, red dots) is within the experimental range for mature cells (shown as black points in Fig. 15*B*). The experimental AP data, which was not utilized in fitting the mature model, serves to validate that the mature model is representative of the experimentally matured iPSC-CMs. The resulting mature model diastolic membrane potential ($MDP_{Mature,\,Model} = -77.4$ mV) is representative of the average experimentally matured cells ($MDP_{Mature,\,Exp} = -77.5$ mV) and has a more hyperpolarized diastolic membrane potential than the immature model ($MDP_{Immature,\,Model} = -75.6$ mV). The AP amplitude of the mature model population is larger than the immature model population ($Amp_{Mature,Model} = 108 \pm 6$ mV, $Amp_{Immature,Model} = 90 \pm 9$ mV), which is consistent with the experimentally observed trend of a larger AP amplitude in mature cells ($Amp_{Mature,Exp} = 117 \pm 6$ mV, $Amp_{Immature,Exp} = 105 \pm 16$ mV). Similarly, the APD in the mature population is slightly longer than the immature population ($APD_{90,Mature,Model} = 347 \pm 77$ ms, $APD_{90,Immature,Model} = 340 \pm 74$ ms), which is consistent with the experimental results ($APD_{90,Mature,Exp} = 453 \pm 113$ ms, $APD_{90,Immature,Exp} = 437 \pm 173$ ms). Finally, for maximal upstroke velocity (dV/dt), the mature model value ($dV/dt_{Mature,Model} = 199$ mV ms^{-1}) is within the experimentally measured range ($dV/dt_{Mature,Exp} = 147 \pm 87$ mV ms^{-1}) and has a much higher upstroke velocity than the immature model value ($dV/dt_{Immature,Model} = 33$ mV ms^{-1}), as would be expected in a more mature cell.

Maturation: population-based insights

Notably, experimentally recorded mature iPSC-CMs retained spontaneous beating, although our mature model cells required stimulation to beat. This indicates that there was either an excess of I_{K1} in our representative mature model, or that other currents compensate for the increased I_{K1}, allowing the mature experimental cells to retain spontaneous beating at more negative maximum diastolic potentials. This led us to analyse our population of spontaneous beating cells and explore a computational subpopulation of cells that exhibited a mature phenotype, at the same time as retaining spontaneous beating. One of the advantages of a population-based modelling approach is the ability to utilize a component dissection approach to identify plausible ionic mechanisms of known phenotypes. As a test case, we examined the immature and mature phenotypes in our model iPSC-CM population. We formed two subpopulations of cells from the five-current variation population (Fig. 13*B*), based on phenotype. Based on the experimental data from the Jalife Lab, we determined ranges of cellular MDP and maximal upstroke velocity outputs that defined our immature and mature model subpopulations. The cut-off regions for MDP and upstroke velocity were determined based on the experimental outputs for matured cells (black points, Fig. 16*A*) compared to control cells, which exhibit a more immature phenotype (Fig. 16*A*, open circles). We categorized mature cells as those with hyperpolarized diastolic potentials and high upstroke velocity (MDP <-75 mV, $dv/dt_{max} > 85$ mV ms^{-1}) (Fig. 16*A*, red) and immature cells as those with depolarized diastolic potentials and low upstroke velocity (MDP >-75 mV, $dv/dt_{max} < 85$ mV ms^{-1}) (Fig. 16*A*, blue). A third group of cellular models that did not meet either the immature

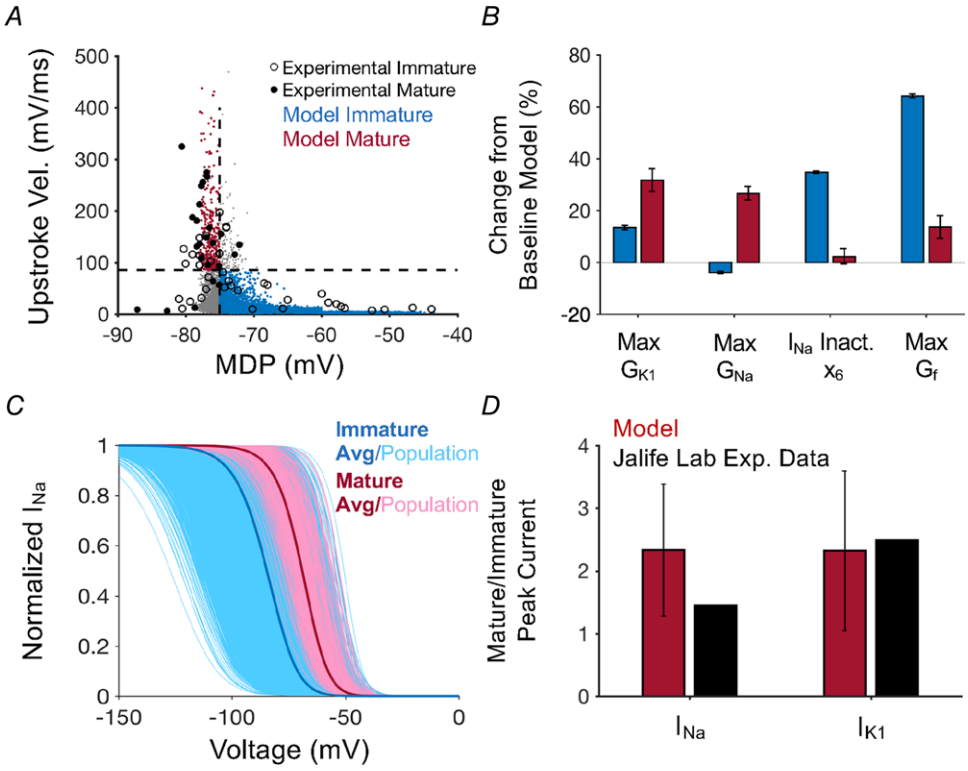

Figure 16. Comparison of mature and immature iPSC-CM model subpopulations
A, division of model population into mature and immature phenotypes (using five-current variation population with simultaneous variation in I_{Na}, I_{CaL}, I_{Kr}, I_F and I_{K1} parameters). Experimental data are from the Jalife Lab (Herron *et al.* 2016). Model subpopulation shown in red ($n = 325$) represents mature phenotypes with MDP <-75 mV and maximal upstroke velocity >85 V s^{-1}. The model subpopulation shown in blue ($n = 13\,759$) represents immature phenotypes with MDP >-75 mV and maximal upstroke velocity <85 V s^{-1}. The model subpopulation shown in grey was not analysed in this comparison. *B*, the four model parameters with the largest difference between the mature and immature model subpopulations. For each subpopulation, parameter averages and SDs are shown as the percentage change from the baseline model parameter value. *C*, steady-state inactivation for I_{Na} in the mature and immature model subpopulations. Individual cells (light colours) and subpopulation average parameter values (darker colored lines) are shown. *D*, peak I_{K1} and I_{Na} for the *I–V* relationship of each cell in the model subpopulations were compared with data reported in Herron *et al.* (2016). Model and experimental values are shown as the percentage change from the immature to mature phenotype.

or mature phenotype criteria (Fig. 16*A*, grey) were not analysed.

To compare mature and immature populations, we looked at the underlying model parameters that had the largest difference between the two populations. To normalize parameter values, the population analysis was conducted using percentage change in parameter value from the baseline model parameter value, shown in Fig. 16*B*. The three currents identified in this analysis were I_{K1}, I_{Na} and I_f. Maximal conductance parameters for all three currents were identified, with lower maximal conductance of I_{K1} and I_{Na} found in the immature cells, which is consistent with the findings in Herron *et al.* (2016). Both currents are directly related to the defining characteristics of mature and immature sub-populations because increased I_{K1} hyperpolarized the MDP and increased I_{Na} increased the maximal upstroke velocity. In addition to g_{K1} and g_{Na}, the immature population also exhibited increased g_f, which is consistent with an immature cardiomyocyte phenotype (Karakikes *et al.* 2015; Kim *et al.* 2015).

In additional to maximal conductances, x_6 in the formulation of the I_{Na} inactivation gate was also identified. The decrease in the x_6 parameter impacts the shift in the I_{Na} inactivation (h and j) steady-state curves, as described in the Methods; see eqns (8)–(9). A decrease in x_6 in the mature models corresponds to increased I_{Na} in the physiological voltage range by shifting the steady-state inactivation curve toward the physiological range, as shown for the model populations in Fig. 16*C* (individual models in light colours, population averages in dark colours). Similarly, x_6 shifts the negatively sloped portion of the time constant of decay curve, causing an increased time constant of inactivation in the relevant range for the upstroke of the AP (−70 to −50 mV). An increase in time constant slows the inactivation of I_{Na}. Collectively, this change in x_6 results in more I_{Na} during the upstroke of the AP, demonstrating a combined impact with the increase in g_{Na} in mature cells, which all contribute to the increased maximal upstroke velocity. Additionally, Fig. 16*C* shows that there are immature cells (Fig. 16*C*, blue) with steady-state inactivation curves resulting in V_{half} in the mature range (−85 to −50 mV) but no mature cells (Fig. 16*C*, pink) with V_{half} <−85 mV. This suggests that, to reach a maximal upstroke velocity >85 mV ms^{-1}, our cut-off for mature cells, the cellular I_{Na} model needs to fall within a smaller range of steady-state inactivation behaviours. This positive shift in the inactivation curve, and a corresponding increase in g_{Na} (Fig. 16*B*), allows for a large influx of I_{Na} during the AP upstroke, resulting in a more mature phenotype with a high upstroke velocity. Immature cells with low maximal upstroke velocity have a much wider range of steady-state inactivation curves that are compensated by a wide range of maximal I_{Na} conductance values to keep the upstroke velocity within the immature range. It should be noted that the baseline model can maintain spontaneous beating with complete I_{Na} block, as has been shown experimentally in iPSC-CMs (Guo *et al.* 2011; Sheng *et al.* 2012). Thus, some cells in immature population may have I_{Na} parameterizations that result in a miniscule I_{Na} during spontaneous beating.

The population-based approach identified three currents (I_{Na}, I_{K1} and I_f) that are appreciably different between the immature and mature subpopulations (Fig. 16*B*). Two of these currents have been experimentally validated by the Jalife Lab, as shown in Fig. 16*D*. Experimental measurements in matured iPSC-CMs show enhanced I_{Na} and I_{K1} compared to the control cells. The experimental and *in silico* results are shown in Fig. 16*D* for the mature cells. The mature cellular outputs were normalized to the respective average experimental or *in silico* immature outputs. In the model subpopulations, the peak current from the *I–V* curve for each cell in the mature population was normalized to the mean value of the peak current in the immature population. For I_{K1}, we analysed the outward portion I_{K1}, which occurs in the physiological voltage range (V_m >85 mV) for iPSC-CMs.

Although the MDP and upstroke velocity are known to be directly linked to the maximal conductance of I_{K1} and I_{Na}, respectively, this methodology also identified g_f and the kinetics of I_{Na} that contribute to the mature phenotype. In the future, this approach can also be expanded to identify mechanisms of disease states. The data used to construct this model were from presumed healthy iPSC-CMs, although a similar approach could be used to identify molecular mechanisms of increased proclivity to arrhythmia or susceptibility to proarrhythmic drugs in a diseased population model.

Discussion

In the present study, we present a modelling approach for *in silico* representation of iPSC-CMs. We used a 'bottom-up' approach by developing models of sub-cellular components, namely individual ionic currents and Ca^{2+} handling proteins. The study was conducted in collaboration with a number of experimental laboratories who generously provided data recorded from iPSC-CMs in their respective laboratories. These data allowed us to consider measured variability in ionic currents and their underlying processes. To minimize the number of model parameters, as well as to prevent overfitting, we utilized a simple formulation of the ionic currents with fewer parameters than other commonly used cardiomyocyte or ionic current models (ten Tusscher *et al.* 2004; Moreno *et al.* 2011; O'Hara *et al.* 2011).

To gain a complete representation of the behaviour of iPSC-CMs, a single average behaviour is insufficient. There is no experimental consensus on which iPSC-CM

recording might represent average or representative behaviour. We aimed to determine whether variability at the subcellular level was sufficient to replicate this wide range of whole-cell iPSC-CM phenotypes. Figure 13*D–F* shows that our *in silico* population, informed purely by the distribution of experimentally observed kinetic behaviour, reproduces the range of whole-cell behaviours observed experimentally. Within this population, each individual model, including the baseline model, is presumed to be an equally valid representation of an iPSC-CM.

In developing a collection of *in silico* iPSC-CMs that reflect phenotypic cellular variability, we explored populations with single current variation, as well as simultaneous variation in five key currents. Although the five-current variation population provides the most complete coverage of the experimentally observed parameter space, comparing the different populations developed can provide additional insight (Fig. 13). For each of the single-current variation populations, there is a relatively narrow range of variability in whole-cell AP morphology. Additionally, almost all of the models created through single current variation resulted in a viable and spontaneously beating cellular model. However, when variation in multiple currents was included in the cell representation, there was a much larger range of AP morphologies including 'non-viable' *in silico* iPSC-CMs that were not possible to excite or did not repolarize.

The results described above are not surprising and may stem from physiologically relevant regulatory phenomena that require correlation and co-ordination of ionic currents within individual cells. For example, to have sufficient net repolarizing current during the AP, there must be a mechanism of coregulation for repolarizing currents (Xiao *et al.* 2008; Varro & Baczko, 2011). In iPSC-CMs, and other fetal-like cell types, there is a particularly low density of I_{K1} compared to adult cardiomyocytes (Bett *et al.* 2013; Meijer van Putten *et al.* 2015; Vaidyanathan *et al.* 2016). Although our cellular populations include a large range of variation in I_{K1}, there is much lower I_{K1} density throughout these populations than there would be in an adult ventricular cardiomyocyte (Karakikes *et al.* 2015). In particular, the lack of I_{K1} plays a key role in the spontaneously beating phenotype, which is characteristic of these cells (Kim *et al.* 2015). Thus, there is a balance of repolarizing currents in iPSC-CMs that allow for spontaneous beating, at the same time as maintaining the cells ability to fully repolarize. Because every cell in our a populations maintains spontaneous beating (Fig. 13), every cell also requires the coregulation of ionic current density that maintains a unique balance of repolarizing currents to accommodate the relatively low I_{K1}.

Coregulation has been shown experimentally in numerous studies of cardiac cells (Deschenes *et al.* 2008; Xiao *et al.* 2008; Milstein *et al.* 2012). For example, Liu *et al.* (2016) showed that there is cotranslation of protein subunits, leading to functional regulation of cellular ionic currents within a single cell. Cotranslation may also serve as a mechanism to maintain the balance of ionic currents within a single cell. Banyasz *et al.* (2011) showed that there is a mechanism by which individual cells regulate net ionic current, despite a wide range of variability in density of individual currents. Specifically, there was a linear relationship between the inward and outward currents measured via AP dissection, indicating a mechanism of cellular co-ordination between key inward and outward currents. The results of our population-based studies suggest a similar co-ordination in the ionic currents of iPSC-CMs, allowing for a wide range of variation in subcellular mechanisms at the same time as maintaining functional AP dynamics. Intriguingly, a recent combined computational and experimental study revealed that variable inward calcium and outward potassium currents in mouse ventricular myocytes compensate for each other to generate normal calcium transients and contractile responses (Rees *et al.* 2018). This suggests that a feedback mechanism sensing global cytosolic calcium levels might be sufficient to regulate ionic conductances. Clinically, genetic modifiers have been seen to modify the severity of long QT syndrome type 2. Patients with the same hERG mutations have differential severity in QT prolongation, depending on the presence of other mutations that coregulate cellular repolarization (Chai *et al.* 2018). The present study provides a framework that can be expanded to elucidate these types of feedback and coregulation mechanisms in iPSC-CMs, which directly relate to mechanisms of adult human cardiomyocyte behaviour.

Sources of cellular variation are often unclear, although experimental manipulation allows us to directly compare known sources of variation. Using data from experimentally manipulated cells, we were able to validate our framework for determining sources of variation leading to known phenotypes. The use of data from maturation promoted iPSC-CMs allowed us to conduct a two-pronged analysis of cell maturation. Beginning with a bottom-up approach, we showed that a single cell model can accurately predict a more mature phenotype based on known sources of variation, as shown in Fig. 15. Additionally, we used a top-down approach to test whether the parameter space used to randomly generate our model populations covered the subcellular range of maturation behaviour. As hypothesized, the whole-cell behaviour within the population predicts a range of maturation, as shown in Fig. 16*A*. Additionally, our population-based approach identified the same changes in key currents (I_{Na} and I_{K1}) (Fig. 16*D*) when stratifying subpopulations of mature and immature cellular models.

This same top-down approach can be used to compare other subpopulations. We also used this approach to compare atrial and ventricular-like subpopulations. To

define atrial and ventricular-like subpopulations, we used a metric used experimentally to classify iPSC-CMs: $APD_r = (APD_{40} - APD_{30})/(APD_{80} - APD_{70})$ (Ma *et al.* 2011). Ventricular-like cells are defined as $APD_r > 1.5$, and atrial-like cells are defined as $APD_r < 1.5$. Using the atrial and ventricular-like subpopulations, we conducted the same analysis shown in Fig. 16*B*. Our analysis on the atrial and ventricular-like populations identified the maximal conductance parameters for I_{Kr} and I_{CaL} as having the largest differences between the two subpopulations. This is consistent with experimental works by Lieu *et al.* (2013) in embryonic stem cell-derived cardiomyocytes (ESC-CMs), which identified the increased I_{Kr} and I_{CaL} in ventricular-like compared to atrial-like ESC-CMs. They additionally showed decreased I_f in atrial-like ESC-CMs, which our analysis did not identify. The APD_r criterion was used to define the atrial and ventricular-like subpopulations to be consistent with the experimental methodology, and to show that our model captures these experimental results. However, there is debate over the precision of this definition of atrial *vs.* ventricular cells (Du *et al.* 2015; Giles & Noble, 2016). This criterion considers only the AP morphology with repsect to determining the chamber specificity of the cells, which ignores many other key physiological differences between the two cell types.

The large range of experimentally observed variability in iPSC-CMs, which is recapitulated within the populations of models described in the present study, allows us to examine the mechanistic origin of phenotypic differences (Sarkar & Sobie, 2011; Yang *et al.* 2015; Morotti & Grandi, 2017; Passini *et al.* 2017). Properly utilized, the phenotypic variation in iPSC-CMs can be a strength of this experimental approach, allowing us to better understand the mechanistic underpinnings of phenotypic diversity, which is of course also observed in patients. iPSC-CMs in conjunction with computational approaches provide a unique opportunity to conduct high throughput component dissection of phenotypes of interest, which ultimately can be linked to patient-specific phenotypes.

The present study can also serve as a basis to 'translate' the patient-specific iPSC-CM behaviours from the immature fetal-like phenotype to a predictive model of adult cardiomyocyte behaviour. As has been noted experimentally, our model population reflects the differences in AP morphology between iPSC-CMs and adult ventricular cells. On average, our model population has a more positive resting membrane potential, slower AP upstroke velocity, slower CaT time to peak and reduced CaT amplitude compared to adult ventricular cell models (ten Tusscher *et al.* 2004; O'Hara *et al.* 2011). Understanding the mechanisms of these differences is the first step to translating between iPSC-CM and the adult cardiac response. Critical differences between ionic currents in adult and iPSC-CM have been noted in computational and experimental studies (Karakikes *et al.* 2015; Paci *et al.* 2015). Translation between iPSC-CM and adult phenotypes will be critical with respect to the use of iPSC-CMs for drug safety and discovery in the human population. Gong & Sobie (2018) have developed a cross-cell type regression model that translates response to ionic current perturbations in an iPSC-CM model to the predicted the response in an adult ventricular cardiomyocyte model. Additionally, Tveito *et al.* (2018) have developed a method of utilizing optically obtained experimental whole-cell drug-response data from immature iPSC-CMs to computationally predict the effect in a mature iPSC-CM phenotype, which serves as a more representative model of adult cardiomyocytes. In the future, these computational translation approaches can be coupled with our utilization of experimental data from multiple sources to further reconcile the phenotypic variability observed across iPSC-CM datasets with patient-specific adult cardiac phenotypes.

Limitations

In part, the goal of this modelling approach was to fully parameterize a model from experimental data with the fewest parameters possible and still recapitulate complex behaviour that has been characterized in iPSC-CMs. However, it should be noted that there is no complete experimental characterization of calcium handling, sodium handling or E-C coupling in iPSC-CMs. This a critical point of concern with respect to the adaptation of iPSC-CMs in the study of drug and disease mechanisms. Furthermore, pumps and exchangers also lack experimental characterization in iPSC-CMs. We have modelled the iPSC-CM calcium handling based on all of the available experimental data, resulting in a more experimentally-based iPSC-CM calcium handling than prior modelling efforts. Our model captures the physiological reality for SR-calcium release dependent on cytosolic concentration, faithfully reproduces the experimentally measured contribution of various calcium removal processes, and utilizes experimentally-based calcium buffering parameters. Moreover, we are confident in the validity of adopting earlier model formulations of pumps and exchangers because these mechanisms maintain intrinsic transport stoichiometry and kinetics across various cells. Nonetheless, the implementation of phenomena that are not fully experimentally characterized in iPSC-CMs remains a limitation of our model.

Additionally, an essential gap in knowledge remains related to the source of observed experimental variation. Because some of this variation may come from the cell-culture process or the cell-type, in future work, it would be beneficial to collect a full kinetic characterization of individual cells. A necessary next step is to fully parameterize a cellular model based on the kinetics of individual cells. This future goal will be required

utilization of iPSC-CMs for the pursuit of patient-specific models.

Conclusions

We have utilized multiple iPSC-CM ion channel data sources to construct a range of ion channel models for key iPSC-CM currents. We then utilized random selection of parameters from within the model ranges to inform development of a population of cellular level iPSC-CM models. Several conclusions can be drawn: (i) variation in the underlying model parameters within the experimentally measured ranges were sufficient to encapsulate the complete diverse range of whole-cell iPSC-CM phenotypes that are observed experimentally; (ii) this method of deriving a population of model cells obviated the need for 'calibration' or selecting models that exhibit physiologically relevant electrical behaviour, beyond excluding non-excitable or non-repolarizing cells; and (iii) mature and immature iPSC-CM phenotypes naturally emerge as subsets of the population.

The construction described in the presented study has many potential future applications that can aid our understanding of cardiac disease and drug testing. In conjunction with the existing CiPA protocol (Cavero & Holzgrefe, 2014), the iPSC-CM computational model in the present study can be applied to provide a better understanding of the parameter combinations that lead to proarrhythmic behaviours. This *in silico* population-based framework for analysing the iPSC-CM phenotype has the added advantage of being a high throughput analysis tool. Additionally, the models that we present can be readily expanded to include genetic mutations, pharmacological interventions, sex-based differences and a variety of perturbations. Future studies could utilize coupled sheets of *in silico* tissue to test higher dimension arrhythmia proclivity and sustainability.

References

Banyasz T, Horvath B, Jian Z, Izu LT & Chen-Izu Y (2011). Sequential dissection of multiple ionic currents in single cardiac myocytes under action potential-clamp. *J Mol Cell Cardiol* **50**, 578–581.

Beeler GW & Reuter H (1977). Reconstruction of the action potential of ventricular myocardial fibres. *J Physiol* **268**, 177–210.

Behr ER & Roden D (2013). Drug-induced arrhythmia: pharmacogenomic prescribing? *Eur Heart J* **34**, 89–95.

Bellin M, Casini S, Davis RP, D'Aniello C, Haas J, Ward-van Oostwaard D, Tertoolen LG, Jung CB, Elliott DA, Welling A, Laugwitz KL, Moretti A & Mummery CL (2013). Isogenic human pluripotent stem cell pairs reveal the role of a KCNH2 mutation in long-QT syndrome. *EMBO J* **32**, 3161–3175.

Bers DM (2000). Calcium fluxes involved in control of cardiac myocyte contraction. *Circ Res* **87**, 275–281.

Bett GC, Kaplan AD, Lis A, Cimato TR, Tzanakakis ES, Zhou Q, Morales MJ & Rasmusson RL (2013). Electronic 'expression' of the inward rectifier in cardiocytes derived from human-induced pluripotent stem cells. *Heart Rhythm* **10**, 1903–1910.

Britton OJ, Bueno-Orovio A, Van Ammel K, Lu HR, Towart R, Gallacher DJ & Rodriguez B (2013). Experimentally calibrated population of models predicts and explains intersubject variability in cardiac cellular electrophysiology. *Proc Natl Acad Sci U S A* **110**, E2098–2105.

Burridge PW, Li YF, Matsa E, Wu H, Ong SG, Sharma A, Holmstrom A, Chang AC, Coronado MJ, Ebert AD, Knowles JW, Telli ML, Witteles RM, Blau HM, Bernstein D, Altman RB & Wu JC (2016). Human induced pluripotent stem cell-derived cardiomyocytes recapitulate the predilection of breast cancer patients to doxorubicin-induced cardiotoxicity. *Nat Med* **22**, 547–556.

Cavero I & Holzgrefe H (2014). Comprehensive in vitro proarrhythmia assay, a novel in vitro/in silico paradigm to detect ventricular proarrhythmic liability: a visionary 21st century initiative. *Expert Opin Drug Saf* **13**, 745–758.

Chai S, Wan X, Ramirez-Navarro A, Tesar PJ, Kaufman ES, Ficker E, George AL, Jr. & Deschenes I (2018). Physiological genomics identifies genetic modifiers of long QT syndrome type 2 severity. *J Clin Invest* **128**, 1043–1056.

Cordeiro JM, Nesterenko VV, Sicouri S, Goodrow RJ, Jr., Treat JA, Desai M, Wu Y, Doss MX, Antzelevitch C & Di Diego JM (2013). Identification and characterization of a transient outward K+ current in human induced pluripotent stem cell-derived cardiomyocytes. *J Mol Cell Cardiol* **60**, 36–46.

Correa AM, Latorre R & Bezanilla F (1991). Ion permeation in normal and batrachotoxin-modified Na^+ channels in the squid giant axon. *J Gen Physiol* **97**, 605–625.

DeBoever C, Li H, Jakubosky D, Benaglio P, Reyna J, Olson KM, Huang H, Biggs W, Sandoval E, D'Antonio M, Jepsen K, Matsui H, Arias A, Ren B, Nariai N, Smith EN, D'Antonio-Chronowska A, Farley EK & Frazer KA (2017). Large-scale profiling reveals the influence of genetic variation on gene expression in human induced pluripotent stem cells. *Cell Stem Cell* **20**, 533–546 e537.

Deschenes I, Armoundas AA, Jones SP & Tomaselli GF (2008). Post-transcriptional gene silencing of KChIP2 and Navbeta1 in neonatal rat cardiac myocytes reveals a functional association between Na and Ito currents. *J Mol Cell Cardiol* **45**, 336–346.

DiFrancesco D & Noble D (1985). A model of cardiac electrical activity incorporating ionic pumps and concentration changes. *Philos Trans R Soc Lond B Biol Sci* **307**, 353–398.

Doss MX, Di Diego JM, Goodrow RJ, Wu Y, Cordeiro JM, Nesterenko VV, Barajas-Martinez H, Hu D, Urrutia J, Desai M, Treat JA, Sachinidis A & Antzelevitch C (2012). Maximum diastolic potential of human induced pluripotent stem cell-derived cardiomyocytes depends critically on I(Kr). *PLoS ONE* **7**, e40288.

Du DTM, Hellen N, Kane C & Terracciano CMN (2015). Action potential morphology of human induced pluripotent stem cell-derived cardiomyocytes does not predict cardiac chamber specificity and is dependent on cell density. *Biophys J* **108**, 1–4.

Es-Salah-Lamoureux Z, Jouni M, Malak OA, Belbachir N, Al Sayed ZR, Gandon-Renard M, Lamirault G, Gauthier C, Baro I, Charpentier F, Zibara K, Lemarchand P, Beaumelle B, Gaborit N & Loussouarn G (2016). HIV-Tat induces a decrease in IKr and IKsvia reduction in phosphatidylinositol-(4,5)-bisphosphate availability. *J Mol Cell Cardiol* **99**, 1–13.

Fermini B, Hancox JC, Abi-Gerges N, Bridgland-Taylor M, Chaudhary KW, Colatsky T, Correll K, Crumb W, Damiano B, Erdemli G, Gintant G, Imredy J, Koerner J, Kramer J, Levesque P, Li Z, Lindqvist A, Obejero-Paz CA, Rampe D, Sawada K, Strauss DG & Vandenberg JI (2016). A new perspective in the field of cardiac safety testing through the comprehensive in vitro proarrhythmia assay paradigm. *J Biomol Screen* **21**, 1–11.

Garg P, Oikonomopoulos A, Chen H, Li Y, Lam CK, Sallam K, Perez M, Lux RL, Sanguinetti MC & Wu JC (2018). Genome editing of induced pluripotent stem cells to decipher cardiac channelopathy variant. *J Am Coll Cardiol* **72**, 62–75.

Gibson JK, Yue Y, Bronson J, Palmer C & Numann R (2014). Human stem cell-derived cardiomyocytes detect drug-mediated changes in action potentials and ion currents. *J Pharmacol Toxicol Methods* **70**, 255–267.

Giles WR & Noble D (2016). Rigorous phenotyping of cardiac iPSC preparations requires knowledge of their resting potential(s). *Biophys J* **110**, 278–280.

Gong JQX & Sobie EA (2018). Population-based mechanistic modeling allows for quantitative predictions of drug responses across cell types. *NPJ Syst Biol Appl* **4**, 11.

Guo L, Abrams RM, Babiarz JE, Cohen JD, Kameoka S, Sanders MJ, Chiao E & Kolaja KL (2011). Estimating the risk of drug-induced proarrhythmia using human induced pluripotent stem cell-derived cardiomyocytes. *Toxicol Sci* **123**, 281–289.

Harris K, Aylott M, Cui Y, Louttit JB, McMahon NC & Sridhar A (2013). Comparison of electrophysiological data from human-induced pluripotent stem cell-derived cardiomyocytes to functional preclinical safety assays. *Toxicol Sci* **134**, 412–426.

Herron TJ, Rocha AM, Campbell KF, Ponce-Balbuena D, Willis BC, Guerrero-Serna G, Liu Q, Klos M, Musa H, Zarzoso M, Bizy A, Furness J, Anumonwo J, Mironov S & Jalife J (2016). Extracellular matrix-mediated maturation of human pluripotent stem cell-derived cardiac monolayer structure and electrophysiological function. *Circ Arrhythm Electrophysiol* **9**, e003638.

Hodgkin AL & Huxley AF (1952). A quantitative description of membrane current and its application to conduction and excitation in nerve. *J Physiol* **117**, 500–544.

Hortigon-Vinagre MP, Zamora V, Burton FL, Green J, Gintant GA & Smith GL (2016). The use of ratiometric fluorescence measurements of the voltage sensitive dye di-4-ANEPPS to examine action potential characteristics and drug effects on human induced pluripotent stem cell-derived cardiomyocytes. *Toxicol Sci* **154**, 320–331.

Hwang HS, Kryshtal DO, Feaster TK, Sanchez-Freire V, Zhang J, Kamp TJ, Hong CC, Wu JC & Knollmann BC (2015). Comparable calcium handling of human iPSC-derived cardiomyocytes generated by multiple laboratories. *J Mol Cell Cardiol* **85**, 79–88.

Itzhaki I, Maizels L, Huber I, Zwi-Dantsis L, Caspi O, Winterstern A, Feldman O, Gepstein A, Arbel G, Hammerman H, Boulos M & Gepstein L (2011). Modelling the long QT syndrome with induced pluripotent stem cells. *Nature* **471**, 225–229.

Ivashchenko CY, Pipes GC, Lozinskaya IM, Lin Z, Xiaoping X, Needle S, Grygielko ET, Hu E, Toomey JR, Lepore JJ & Willette RN (2013). Human-induced pluripotent stem cell-derived cardiomyocytes exhibit temporal changes in phenotype. *Am J Physiol Heart Circ Physiol* **305**, H913–H922.

Jamshidi Y, Nolte IM, Dalageorgou C, Zheng D, Johnson T, Bastiaenen R, Ruddy S, Talbott D, Norris KJ, Snieder H, George AL, Marshall V, Shakir S, Kannankeril PJ, Munroe PB, Camm AJ, Jeffery S, Roden DM & Behr ER (2012). Common variation in the NOS1AP gene is associated with drug-induced QT prolongation and ventricular arrhythmia. *J Am Coll Cardiol* **60**, 841–850.

Jonsson MK, Vos MA, Mirams GR, Duker G, Sartipy P, de Boer TP & van Veen TA (2012). Application of human stem cell-derived cardiomyocytes in safety pharmacology requires caution beyond hERG. *J Mol Cell Cardiol* **52**, 998–1008.

Kaab S, Crawford DC, Sinner MF, Behr ER, Kannankeril PJ, Wilde AA, Bezzina CR, Schulze-Bahr E, Guicheney P, Bishopric NH, Myerburg RJ, Schott JJ, Pfeufer A, Beckmann BM, Martens E, Zhang T, Stallmeyer B, Zumhagen S, Denjoy I, Bardai A, Van Gelder IC, Jamshidi Y, Dalageorgou C, Marshall V, Jeffery S, Shakir S, Camm AJ, Steinbeck G, Perz S, Lichtner P, Meitinger T, Peters A, Wichmann HE, Ingram C, Bradford Y, Carter S, Norris K, Ritchie MD, George AL, Jr. & Roden DM (2012). A large candidate gene survey identifies the KCNE1 D85N polymorphism as a possible modulator of drug-induced torsades de pointes. *Circ Cardiovasc Genet* **5**, 91–99.

Kamakura T, Makiyama T, Sasaki K, Yoshida Y, Wuriyanghai Y, Chen J, Hattori T, Ohno S, Kita T, Horie M, Yamanaka S & Kimura T (2013). Ultrastructural maturation of human-induced pluripotent stem cell-derived cardiomyocytes in a long-term culture. *Circ J* **77**, 1307–1314.

Karakikes I, Ameen M, Termglinchan V & Wu JC (2015). Human induced pluripotent stem cell-derived cardiomyocytes: insights into molecular, cellular, and functional phenotypes. *Circ Res* **117**, 80–88.

Karakikes I, Termglinchan V & Wu JC (2014). Human-induced pluripotent stem cell models of inherited cardiomyopathies. *Curr Opin Cardiol* **29**, 214–219.

Kim JJ, Yang L, Lin B, Zhu X, Sun B, Kaplan AD, Bett GC, Rasmusson RL, London B & Salama G (2015). Mechanism of automaticity in cardiomyocytes derived from human induced pluripotent stem cells. *J Mol Cell Cardiol* **81**, 81–93.

Kiyosue T, Arita M, Muramatsu H, Spindler AJ & Noble D (1993). Ionic mechanisms of action potential prolongation at low temperature in guinea-pig ventricular myocytes. *J Physiol* **468**, 85–106.

Koivumaki JT, Naumenko N, Tuomainen T, Takalo J, Oksanen M, Puttonen KA, Lehtonen S, Kuusisto J, Laakso M, Koistinaho J & Tavi P (2018). Structural immaturity of human iPSC-derived cardiomyocytes: in silico investigation of effects on function and disease modeling. *Front Physiol* **9**, 80.

Kurokawa J, Motoike HK & Kass RS (2001). TEA(+)-sensitive KCNQ1 constructs reveal pore-independent access to KCNE1 in assembled I(Ks) channels. *J Gen Physiol* **117**, 43–52.

Lan F, Lee AS, Liang P, Sanchez-Freire V, Nguyen PK, Wang L, Han L, Yen M, Wang Y, Sun N, Abilez OJ, Hu S, Ebert AD, Navarrete EG, Simmons CS, Wheeler M, Pruitt B, Lewis R, Yamaguchi Y, Ashley EA, Bers DM, Robbins RC, Longaker MT & Wu JC (2013). Abnormal calcium handling properties underlie familial hypertrophic cardiomyopathy pathology in patient-specific induced pluripotent stem cells. *Cell Stem Cell* **12**, 101–113.

Lei CL, Wang K, Clerx M, Johnstone RH, Hortigon-Vinagre MP, Zamora V, Allan A, Smith GL, Gavaghan DJ, Mirams GR & Polonchuk L (2017). Tailoring mathematical models to stem-cell derived cardiomyocyte lines can improve predictions of drug-induced changes to their electrophysiology. *Front Physiol* **8**, 986.

Leopold JA & Loscalzo J (2018). Emerging role of precision medicine in cardiovascular disease. *Circ Res* **122**, 1302–1315.

Li M, Kanda Y, Ashihara T, Sasano T, Nakai Y, Kodama M, Hayashi E, Sekino Y, Furukawa T & Kurokawa J (2017). Overexpression of KCNJ2 in induced pluripotent stem cell-derived cardiomyocytes for the assessment of QT-prolonging drugs. *J Pharmacol Sci* **134**, 75–85.

Liang P, Lan F, Lee AS, Gong T, Sanchez-Freire V, Wang Y, Diecke S, Sallam K, Knowles JW, Wang PJ, Nguyen PK, Bers DM, Robbins RC & Wu JC (2013). Drug screening using a library of human induced pluripotent stem cell-derived cardiomyocytes reveals disease-specific patterns of cardiotoxicity. *Circulation* **127**, 1677–1691.

Lieu DK, Fu JD, Chiamvimonvat N, Tung KC, McNerney GP, Huser T, Keller G, Kong CW & Li RA (2013). Mechanism-based facilitated maturation of human pluripotent stem cell-derived cardiomyocytes. *Circ Arrhythm Electrophysiol* **6**, 191–201.

Liu F, Jones DK, de Lange WJ & Robertson GA (2016). Cotranslational association of mRNA encoding subunits of heteromeric ion channels. *Proc Natl Acad Sci U S A* **113**, 4859–4864.

Luo CH & Rudy Y (1994). A dynamic model of the cardiac ventricular action potential. I. Simulations of ionic currents and concentration changes. *Circ Res* **74**, 1071–1096.

Ma D, Wei H, Lu J, Huang D, Liu Z, Loh LJ, Islam O, Liew R, Shim W & Cook SA (2015). Characterization of a novel KCNQ1 mutation for type 1 long QT syndrome and assessment of the therapeutic potential of a novel IKs activator using patient-specific induced pluripotent stem cell-derived cardiomyocytes. *Stem Cell Res Ther* **6**, 39.

Ma J, Guo L, Fiene SJ, Anson BD, Thomson JA, Kamp TJ, Kolaja KL, Swanson BJ & January CT (2011). High purity human-induced pluripotent stem cell-derived cardiomyocytes: electrophysiological properties of action potentials and ionic currents. *Am J Physiol Heart Circ Physiol* **301**, H2006–H2017.

Maltsev VA & Lakatta EG (2009). Synergism of coupled subsarcolemmal Ca^{2+} clocks and sarcolemmal voltage clocks confers robust and flexible pacemaker function in a novel pacemaker cell model. *Am J Physiol Heart Circ Physiol* **296**, H594–H615.

Meijer van Putten RM, Mengarelli I, Guan K, Zegers JG, van Ginneken AC, Verkerk AO & Wilders R (2015). Ion channelopathies in human induced pluripotent stem cell derived cardiomyocytes: a dynamic clamp study with virtual IK1. *Front Physiol* **6**, 7.

Milstein ML, Musa H, Balbuena DP, Anumonwo JM, Auerbach DS, Furspan PB, Hou L, Hu B, Schumacher SM, Vaidyanathan R, Martens JR & Jalife J (2012). Dynamic reciprocity of sodium and potassium channel expression in a macromolecular complex controls cardiac excitability and arrhythmia. *Proc Natl Acad Sci U S A* **109**, E2134–2143.

Moreau A, Mercier A, Theriault O, Boutjdir M, Burger B, Keller DI & Chahine M (2017). Biophysical, molecular, and pharmacological characterization of voltage-dependent sodium channels from induced pluripotent stem cell-derived cardiomyocytes. *Can J Cardiol* **33**, 269–278.

Moreno JD, Lewis TJ & Clancy CE (2016). Parameterization for in-silico modeling of ion channel interactions with drugs. *PLoS ONE* **11**, e0150761.

Moreno JD, Zhu ZI, Yang PC, Bankston JR, Jeng MT, Kang C, Wang L, Bayer JD, Christini DJ, Trayanova NA, Ripplinger CM, Kass RS & Clancy CE (2011). A computational model to predict the effects of class I anti-arrhythmic drugs on ventricular rhythms. *Sci Transl Med* **3**, 98ra83.

Moretti A, Bellin M, Welling A, Jung CB, Lam JT, Bott-Flugel L, Dorn T, Goedel A, Hohnke C, Hofmann F, Seyfarth M, Sinnecker D, Schomig A & Laugwitz KL (2010). Patient-specific induced pluripotent stem-cell models for long-QT syndrome. *N Engl J Med* **363**, 1397–1409.

Morotti S & Grandi E (2017). Logistic regression analysis of populations of electrophysiological models to assess proarrythmic risk. *MethodsX* **4**, 25–34.

Muszkiewicz A, Britton OJ, Gemmell P, Passini E, Sanchez C, Zhou X, Carusi A, Quinn TA, Burrage K, Bueno-Orovio A & Rodriguez B (2016). Variability in cardiac electrophysiology: using experimentally-calibrated populations of models to move beyond the single virtual physiological human paradigm. *Prog Biophys Mol Biol* **120**, 115–127.

Narsinh KH, Sun N, Sanchez-Freire V, Lee AS, Almeida P, Hu S, Jan T, Wilson KD, Leong D, Rosenberg J, Yao M, Robbins RC & Wu JC (2011). Single cell transcriptional profiling reveals heterogeneity of human induced pluripotent stem cells. *J Clin Invest* **121**, 1217–1221.

Navarrete EG, Liang P, Lan F, Sanchez-Freire V, Simmons C, Gong T, Sharma A, Burridge PW, Patlolla B, Lee AS, Wu H, Beygui RE, Wu SM, Robbins RC, Bers DM & Wu JC (2013). Screening drug-induced arrhythmia [corrected] using human induced pluripotent stem cell-derived cardiomyocytes and low-impedance microelectrode arrays. *Circulation* **128**, S3–13.

Ni H, Morotti S & Grandi E (2018). A heart for diversity: simulating variability in cardiac arrhythmia research. *Front Physiol* **9**, 958.

Nunes SS, Miklas JW, Liu J, Aschar-Sobbi R, Xiao Y, Zhang B, Jiang J, Masse S, Gagliardi M, Hsieh A, Thavandiran N, Laflamme MA, Nanthakumar K, Gross GJ, Backx PH, Keller G & Radisic M (2013). Biowire: a platform for maturation of human pluripotent stem cell-derived cardiomyocytes. *Nat Methods* **10**, 781–787.

O'Hara T, Virag L, Varro A & Rudy Y (2011). Simulation of the undiseased human cardiac ventricular action potential: model formulation and experimental validation. *PLoS Comput Biol* **7**, e1002061.

Ono K & Iijima T (2010). Cardiac T-type Ca(2+) channels in the heart. *J Mol Cell Cardiol* **48**, 65–70.

Paci M, Casini S, Bellin M, Hyttinen J & Severi S (2018). Large-scale simulation of the phenotypical variability induced by loss-of-function long QT mutations in human induced pluripotent stem cell cardiomyocytes. *Int J Mol Sci* **19**, pii: E3583.

Paci M, Hyttinen J, Aalto-Setala K & Severi S (2013). Computational models of ventricular- and atrial-like human induced pluripotent stem cell derived cardiomyocytes. *Ann Biomed Eng* **41**, 2334–2348.

Paci M, Hyttinen J, Rodriguez B & Severi S (2015). Human induced pluripotent stem cell-derived versus adult cardiomyocytes: an in silico electrophysiological study on effects of ionic current block. *Br J Pharmacol* **172**, 5147–5160.

Paci M, Passini E, Severi S, Hyttinen J & Rodriguez B (2017). Phenotypic variability in LQT3 human induced pluripotent stem cell-derived cardiomyocytes and their response to antiarrhythmic pharmacologic therapy: an in silico approach. *Heart Rhythm* **14**, 1704–1712.

Paci M, Sartiani L, Del Lungo M, Jaconi M, Mugelli A, Cerbai E & Severi S (2012). Mathematical modelling of the action potential of human embryonic stem cell derived cardiomyocytes. *Biomed Eng Online* **11**, 61.

Passini E, Britton OJ, Lu HR, Rohrbacher J, Hermans AN, Gallacher DJ, Greig RJH, Bueno-Orovio A & Rodriguez B (2017). Human in silico drug trials demonstrate higher accuracy than animal models in predicting clinical pro-arrhythmic cardiotoxicity. *Front Physiol* **8**, 668.

Peng S, Lacerda AE, Kirsch GE, Brown AM & Bruening-Wright A (2010). The action potential and comparative pharmacology of stem cell-derived human cardiomyocytes. *J Pharmacol Toxicol Methods* **61**, 277–286.

Rees CM, Yang JH, Santolini M, Lusis AJ, Weiss JN & Karma A (2018). The Ca(2+) transient as a feedback sensor controlling cardiomyocyte ionic conductances in mouse populations. *Elife* **7**.

Rudy Y & Silva JR (2006). Computational biology in the study of cardiac ion channels and cell electrophysiology. *Q Rev Biophys* **39**, 57–116.

Sallam K, Li Y, Sager PT, Houser SR & Wu JC (2015). Finding the rhythm of sudden cardiac death: new opportunities using induced pluripotent stem cell-derived cardiomyocytes. *Circ Res* **116**, 1989–2004.

Sarkar AX & Sobie EA (2010). Regression analysis for constraining free parameters in electrophysiological models of cardiac cells. *PLoS Comput Biol* **6**, e1000914.

Sarkar AX & Sobie EA (2011). Quantification of repolarization reserve to understand interpatient variability in the response to proarrhythmic drugs: a computational analysis. *Heart Rhythm* **8**, 1749–1755.

Scheel O, Frech S, Amuzescu B, Eisfeld J, Lin KH & Knott T (2014). Action potential characterization of human induced pluripotent stem cell-derived cardiomyocytes using automated patch-clamp technology. *Assay Drug Dev Technol* **12**, 457–469.

Schwartz PJ, Priori SG, Locati EH, Napolitano C, Cantu F, Towbin JA, Keating MT, Hammoude H, Brown AM, Chen LS & Colatsky TJ (1995). Long QT syndrome patients with mutations of the SCN5A and HERG genes have differential responses to Na^+ channel blockade and to increases in heart rate. Implications for gene-specific therapy. *Circulation* **92**, 3381–3386.

Schwartz PJ, Priori SG, Spazzolini C, Moss AJ, Vincent GM, Napolitano C, Denjoy I, Guicheney P, Breithardt G, Keating MT, Towbin JA, Beggs AH, Brink P, Wilde AA, Toivonen L, Zareba W, Robinson JL, Timothy KW, Corfield V, Wattanasirichaigoon D, Corbett C, Haverkamp W, Schulze-Bahr E, Lehmann MH, Schwartz K, Coumel P & Bloise R (2001). Genotype-phenotype correlation in the long-QT syndrome: gene-specific triggers for life-threatening arrhythmias. *Circulation* **103**, 89–95.

Shah M & Carter C (2008). Long QT syndrome: a therapeutic challenge. *Ann Pediatr Cardiol* **1**, 18–26.

Shannon TR, Wang F, Puglisi J, Weber C & Bers DM (2004). A mathematical treatment of integrated Ca dynamics within the ventricular myocyte. *Biophys J* **87**, 3351–3371.

Sheng X, Reppel M, Nguemo F, Mohammad FI, Kuzmenkin A, Hescheler J & Pfannkuche K (2012). Human pluripotent stem cell-derived cardiomyocytes: response to TTX and lidocain reveals strong cell to cell variability. *PLoS ONE* **7**, e45963.

Sobie EA (2009). Parameter sensitivity analysis in electrophysiological models using multivariable regression. *Biophys J* **96**, 1264–1274.

Sun N, Yazawa M, Liu J, Han L, Sanchez-Freire V, Abilez OJ, Navarrete EG, Hu S, Wang L, Lee A, Pavlovic A, Lin S, Chen R, Hajjar RJ, Snyder MP, Dolmetsch RE, Butte MJ, Ashley EA, Longaker MT, Robbins RC & Wu JC (2012). Patient-specific induced pluripotent stem cells as a model for familial dilated cardiomyopathy. *Sci Transl Med* **4**, 130ra147.

Takahashi K & Yamanaka S (2006). Induction of pluripotent stem cells from mouse embryonic and adult fibroblast cultures by defined factors. *Cell* **126**, 663–676.

ten Tusscher KH, Noble D, Noble PJ & Panfilov AV (2004). A model for human ventricular tissue. *Am J Physiol Heart Circ Physiol* **286**, H1573–H1589.

Terrenoire C, Wang K, Tung KW, Chung WK, Pass RH, Lu JT, Jean JC, Omari A, Sampson KJ, Kotton DN, Keller G & Kass RS (2013). Induced pluripotent stem cells used to reveal drug actions in a long QT syndrome family with complex genetics. *J Gen Physiol* **141**, 61–72.

Tiburcy M, Hudson JE, Balfanz P, Schlick S, Meyer T, Chang Liao ML, Levent E, Raad F, Zeidler S, Wingender E, Riegler J, Wang M, Gold JD, Kehat I, Wettwer E, Ravens U, Dierickx P, van Laake LW, Goumans MJ, Khadjeh S, Toischer K, Hasenfuss G, Couture LA, Unger A, Linke WA, Araki T, Neel B, Keller G, Gepstein L, Wu JC & Zimmermann WH (2017). Defined engineered human myocardium with advanced maturation for applications in heart failure modeling and repair. *Circulation* **135**, 1832–1847.

Tveito A, Jaeger KH, Huebsch N, Charrez B, Edwards AG, Wall S & Healy KE (2018). Inversion and computational maturation of drug response using human stem cell derived cardiomyocytes in microphysiological systems. *Sci Rep* **8**, 17626.

Vaidyanathan R, Markandeya YS, Kamp TJ, Makielski JC, January CT & Eckhardt LL (2016). IK1-enhanced human-induced pluripotent stem cell-derived cardiomyocytes: an improved cardiomyocyte model to investigate inherited arrhythmia syndromes. *Am J Physiol Heart Circ Physiol* **310**, H1611–H1621.

Varro A & Baczko I (2011). Cardiac ventricular repolarization reserve: a principle for understanding drug-related proarrhythmic risk. *Br J Pharmacol* **164**, 14–36.

Vassort G, Talavera K & Alvarez JL (2006). Role of T-type Ca^{2+} channels in the heart. *Cell Calcium* **40**, 205–220.

Veerman CC, Mengarelli I, Guan K, Stauske M, Barc J, Tan HL, Wilde AA, Verkerk AO & Bezzina CR (2016). hiPSC-derived cardiomyocytes from Brugada Syndrome patients without identified mutations do not exhibit clear cellular electrophysiological abnormalities. *Sci Rep* **6**, 30967.

Verkerk AO & Wilders R (2013). Hyperpolarization-activated current, If, in mathematical models of rabbit sinoatrial node pacemaker cells. *Biomed Res Int* **2013**, 872454.

Xiao L, Xiao J, Luo X, Lin H, Wang Z & Nattel S (2008). Feedback remodeling of cardiac potassium current expression: a novel potential mechanism for control of repolarization reserve. *Circulation* **118**, 983–992.

Yang PC & Clancy CE (2012). In silico prediction of sex-based differences in human susceptibility to cardiac ventricular tachyarrhythmias. *Front Physiol* **3**, 360.

Yang PC, El-Bizri N, Romero L, Giles WR, Rajamani S, Belardinelli L & Clancy CE (2016). A computational model predicts adjunctive pharmacotherapy for cardiac safety via selective inhibition of the late cardiac Na current. *J Mol Cell Cardiol* **99**, 151–161.

Yang PC, Song Y, Giles WR, Horvath B, Chen-Izu Y, Belardinelli L, Rajamani S & Clancy CE (2015). A computational modelling approach combined with cellular electrophysiology data provides insights into the therapeutic benefit of targeting the late Na^{+} current. *J Physiol* **593**, 1429–1442.

Yang X, Pabon L & Murry CE (2014). Engineering adolescence: maturation of human pluripotent stem cell-derived cardiomyocytes. *Circ Res* **114**, 511–523.

Additional information

Competing interests

The authors declare that they have no competing interests.

Author contributions

DCK, SM, EG and CEC designed the simulations. DCK performed the simulations. HW, PG, HJD, JK, JJ, JCW, EG and CEC designed the experiments. HW, PG, HJD, JK, JJ and JCW performed the experiments. DCK, SM, EG and CEC analysed data. DCK, EG and CEC prepared the manuscript. SM, HW, PG, HJD, JK, JJ and JCW revised the manuscript. EG and CEC co-ordinated and oversaw the project. All authors have approved the final version of the manuscript and agree to be accountable for all aspects of the work. All persons designated as authors qualify for authorship, and all those who qualify for authorship are listed.

Funding

This study was supported by National Institutes of Health NHLBI U01HL126273, R01HL128537, R01HL128170 (to CEC); The National Institutes of Health Common Fund OT2OD026580 (to CEC and EG); American Heart Association grant 15SDG24910015; National Institutes of Health NHLBI R01HL131517, R01HL41214; UC Davis School of Medicine Dean's Fellow award (to EG); National Institutes of Health NHLBI R24HL117756, R01HL113006 (to JCW); National Institutes of Health NHLBI R01HL122352; Grants from Transatlantic Networks of Excellence Program from the Leducq Foundation, and Fondos FEDER, Madrid, Spain (to JJ); NHLBI K99HL138160 award (to SM); and a Predoctoral Fellowship from NIH NHLBI Institutional Training Grant T32HL086350 (to DCK).

Keywords

computer modelling, iPSC-CMs, variability

Translational perspective

Induced pluripotent stem cell-derived cardiomyocytes (iPSC-CMs) have been developed as a promising *in vitro* method for addressing patient-specific proclivity to cardiac disease and drug response. A well-known limitation of iPSC-CMs is the cell-to-cell variability observed in electrical activity. We hypothesize that, when captured in a computational framework, cell-to-cell variability may constitute a useful systems property that can allow the identification of a variety of phenotypic mechanisms and underlying causal components. We have developed a whole-cell model of iPSC-CMs comprising simple model components built on experimental data from multiple laboratories. By including a wide range of input data into the model, we built a population of cellular models to predict robust inter-subject variability in iPSC-CMs. This approach allows for a link between molecular mechanisms and the emergent cellular-level iPSC-CM phenotypes to be revealed. The mechanisms underlying immature and mature subpopulations are predicted and are consistent with the experimental data. In the future, the models presented may prove to be essential for integrating experimental and clinical data from a variety of sources, scales and modalities, allowing high throughput prediction of the link between patient phenotype and patient specific electrophysiology. The tools presented here can be readily expanded and applied for *in silico* screening and the prediction of drug effects on varied genetic backgrounds to predict patient pharmacological responses and even to guide therapy for specific patient therapy.